

**Comment:**

1. Page 9, Line 205-206: it is interesting that in Figure 3, OA in LWC episodes fall into a lower O:C region than those in IR episodes. Does this indicate that the photo-oxidation is more effective to form higher oxidized organics than the aqueous oxidation? While as shown in Fig. 9 of Li et al. (2016), fog, cloud, and rain droplets often contain many highly oxygenated, high molar mass, and low-volatility compounds, indicating aqueous-phase processing can form highly oxidized compounds (Mazzoleni et al., 2010; Zhao et al., 2013). It is helpful to discuss the differences in oxidation state due to photo/aqueous oxidation and compare the oxidation state in this study with previous studies.

**Response:**

We thank the co-Editor for the suggestion to clarify this in the manuscript.

A number of studies (Li et al., 2016; Mazzoleni et al., 2010; Zhao et al., 2013) show that highly oxygenated organic compounds can be formed via aqueous-phase processing. Field measurements as in our case, however, are complicated by primary emissions for analysis of OA during foggy periods because foggy periods were generally associated with stagnant air and accumulated primary emissions. In Y.J. Li et al.(2013), the degree of oxygenation for the overall OA during photochemical oxidation was indeed higher than that in foggy periods characteristic of the aqueous-phase processing. Specifically, we found that the order of degree of oxygenation in this campaign: Hazy > Foggy > Non-fog/Non-haze from the AMS analysis.

However, this might not necessarily mean in general that aqueous processing produces less oxidized OA than photochemical oxidation does. The complication is that a lot of the oxidized OA during foggy periods was scavenged into fog droplets, while AMS only captures the sub-micrometer particles. Even after drying, the AMS will only sample interstitial particles and probably a very small portion of dried fog droplets. In other words, more oxidized species from aqueous-phase processing, if present, might not be captured by AMS during foggy periods. On the other hand, those SOA in hazy periods (mostly photochemical oxidation) are most likely in the sub-micrometer range and are effectively captured by AMS. With these complications, we hesitate to make general statements on how the aging process affects the degree of oxygenation of SOA.

We would like to add a sentence, as below, after "...data points for LWC episodes (blue) fall into a lower O:C region than do the data points for IR (red) and LRT episodes (green)." in the revised manuscript:

"Although aqueous-phase processing might generate highly oxygenated organic compounds (Li et al., 2016; Mazzoleni et al., 2010; Zhao et al., 2013), sampling by the AMS was only limited to interstitial particles and a portion of very small fog droplets after drying. This can also lead to O:C ratios lower than those in IR periods when most of the photochemically oxidized OA were effectively sampled."

**Reference:**

Li, Y., Pöschl, U. and Shiraiwa, M.: Molecular corridors and parameterizations of volatility in the chemical evolution of organic aerosols, *Atmos. Chem. Phys.*, 16(5), 3327–3344, doi:10.5194/acp-16-3327-2016, 2016.

Li, Y. J., Lee, B. Y. L., Yu, J. Z., Ng, N. L. and Chan, C. K.: Evaluating the degree of oxygenation of organic aerosol during foggy and hazy days in Hong Kong using high-resolution time-of-flight aerosol mass spectrometry (HR-ToF-AMS), *Atmos. Chem. Phys.*, 13(17), 8739–8753, doi:10.5194/acp-13-8739-2013, 2013.

Mazzoleni, L. R., Ehrmann, B. M., Shen, X., Marshall, A. G. and Collett, J. L.: Water-Soluble Atmospheric Organic Matter in Fog: Exact Masses and Chemical Formula Identification by Ultrahigh-

Resolution Fourier Transform Ion Cyclotron Resonance Mass Spectrometry, *Environ. Sci. Technol.*, 44(10), 3690–3697, doi:10.1021/es903409k, 2010.

Zhao, Y., Hallar, A. G. and Mazzoleni, L. R.: Atmospheric organic matter in clouds: exact masses and molecular formula identification using ultrahigh-resolution FT-ICR mass spectrometry, *Atmos. Chem. Phys.*, 13(24), 12343–12362, doi:10.5194/acp-13-12343-2013, 2013.

**Particulate matter (PM) episodes at a suburban site in Hong Kong: evolution of PM characteristics and role of photochemistry in secondary aerosol formation**

Yi Ming Qin<sup>1</sup>, Yong Jie Li<sup>2,\*</sup>, Hao Wang<sup>3</sup>, Berto Paul Yok Long Lee<sup>3</sup>, Dan Dan Huang<sup>1</sup>, and Chak Keung Chan<sup>1,3,4,\*</sup>

<sup>1</sup>Department of Chemical and Biomolecular Engineering, Hong Kong University of Science and Technology, Hong Kong, China

<sup>2</sup>Faculty of Science and Technology, University of Macau, Taipa, Macau, China

<sup>3</sup>Division of Environment, Hong Kong University of Science and Technology, Hong Kong, China

<sup>4</sup>School of Energy and Environment, City University of Hong Kong, Hong Kong, China

\*To Whom Correspondence Should be Addressed

Chak K. Chan: AC1-G5716, School of Energy and Environment, City University of Hong Kong,

Tat Chee Avenue, Kowloon, Hong Kong, China

Tel: (852) 3442-5593; Fax: (852) 3442-0688

Email: [chak.k.chan@cityu.edu.hk](mailto:chak.k.chan@cityu.edu.hk)

Yong Jie Li: E11-3017, Faculty of Science and Technology, University of Macau, E11, Avenida da Universidade,

Taipa, Macau, China

Tel: (853) 8822-4943; Fax: (853) 8822-2426

Email: [yongjieli@umac.mo](mailto:yongjieli@umac.mo)

1 **Abstract**

2 Episodes with high concentrations of particulate matter (PM) across the seasons were investigated during four  
3 one-month campaigns at a suburban site in Hong Kong. High-resolution time-of-flight aerosol mass spectrometer  
4 (HR-ToF-AMS) measurements revealed that both regional transport and secondary formation contributed to high  
5 PM levels during the episodes at this site. Based on distinct meteorological conditions, episodes were categorized  
6 into three types: liquid water content (LWC), solar irradiance (IR), and long-range transport (LRT). Despite the  
7 difference in meteorological conditions, all episodes were characterized by a high fraction of sulfate (45%-56%) and  
8 organics (23%-34%). However, aerosols in LWC episodes were less aged, consisting of the lowest fraction of  
9 secondary organics aerosols (SOA) and the highest fraction of small particles. Large particles mixed internally while  
10 freshly formed small particles mixed externally in LWC episodes. Aerosols in LRT episodes, by contrast, were the  
11 most aged and consisted of the highest proportion of low-volatility oxygenated organic aerosols (LVOOA) and the  
12 lowest proportion of small particles. Both small and large particles mixed externally in LRT episodes. The highest  
13 proportion of semi-volatile oxygenated organic aerosols (SVOOA) and a medium proportion of small particles were  
14 observed in IR episodes. Both small and large particles were likely externally mixed during IR episodes. Unlike in  
15 the other two types of episodes, in IR episodes aerosols experienced the most dramatic size increase and diurnal  
16 variation, with a time lag between SVOOA and LVOOA and a gradual increase in carbon oxidation state ( $\overline{OS}_c \approx$   
17  $2 \times O:C-H:C$ ). Five out of ten episodes were of the IR type, further reflecting the importance of this type of episode.  
18 The evolution of aerosol components in one particular episode of the IR type, which exhibited a clear land-sea  
19 breeze pattern, was examined in detail. Sulfate and SOA due to photochemical aging were very efficiently produced  
20 during the course of six hours. The “less-oxidized” SOA (SVOOA) was initially formed at a higher rate than the  
21 “more-oxidized” SOA (LVOOA). The SVOOA transformed to LVOOA at the later stage of photochemical aging.  
22 This transformation was further supported by mass spectral analysis, which showed an increase in the most oxidized  
23 ion ( $CO_2^+$ ) and decreases in moderately oxidized ones ( $C_2H_3O^+$ ,  $C_3H_3O^+$  and  $C_3H_5O^+$ ). By measuring the physical  
24 and chemical properties of PM in a highly time-resolved manner, the current study was able to demonstrate the  
25 dynamic and complex nature of PM transformation during high-PM episodes.

## 26 **1. Introduction**

27 Hong Kong and the rest of the Pearl River Delta (PRD) in China have been battling air pollution episodes as a  
28 result of rapid economic development and urbanization in the region (Ho et al., 2003; Zhong et al., 2013).  
29 Meteorological conditions may govern the regional and long-range transport of air pollutants to Hong Kong. For  
30 example, northerly winds can bring pollutants from the inland areas to Hong Kong, and have been suggested to be  
31 responsible for regional air pollution events in winter (Fang et al., 1999; Huang et al., 2009, 2014b). The majority of  
32 earlier studies used filter sampling with a low time resolution of hours to days, and so were unable to track the  
33 temporal chemical transformation in high particulate matter (PM) episodes. This limitation has hindered our  
34 understanding of the dynamic nature of PM undergoing rapid chemical transformations. Such chemical  
35 transformation can occur within short time periods (e.g., within a day), and so do other physicochemical properties  
36 such as hygroscopic and optical properties. High-time-resolution chemical characterization techniques, for example  
37 the Aerodyne high-resolution time-of-flight aerosol mass spectrometer (HR-ToF-AMS), offer a temporal resolution  
38 of a few minutes. These techniques can thus provide valuable information on rapid changes in the PM composition,  
39 facilitating more detailed analysis of pollution events (Decarlo et al., 2006). HR-ToF-AMS measurements also give  
40 the size distributions of components (DeCarlo et al., 2008; Lee et al., 2013b). These data can reveal the origin,  
41 formation and atmospheric processing mechanisms of PM (Seinfeld and Pandis, 2006; Shiraiwa et al., 2013), but  
42 they remain under-utilized in most aerosol mass spectrometer (AMS) studies.

43 Secondary formation has been recognized as an important route leading to high PM concentrations worldwide  
44 (Zhang et al., 2015a) and is the main culprit for haze episodes in cities across China (Huang et al., 2014a).  
45 Secondary organic aerosol (SOA) has been shown to dominate over primary organic aerosol (POA) after a few  
46 hours of photochemical aging, for instance, in Mexico City (Decarlo et al., 2010; Volkamer et al., 2006), Pasadena  
47 (Hayes et al., 2013) and Tokyo (Takegawa et al., 2006). Semi-volatile oxygenated organic aerosol (SVOOA), which  
48 serves as a proxy for less-oxidized SOA, has been shown to transform to low-volatility oxygenated organic aerosol  
49 (LVOOA), which serves as a proxy for more-oxidized SOA, in laboratory experiments (Alfarra et al., 2012; Jimenez  
50 et al., 2009). Such transformation process may contribute substantially to the accumulation of PM, leading to  
51 episodic events that are frequently observed in the fast-developing city clusters in China (Huang et al., 2012; Zhang  
52 et al., 2015b).

53 We conducted four one-month campaigns in each of the four seasons at the Hong Kong University of Science  
54 and Technology (HKUST) Air Quality Research Supersite (AQRS) from May 2011 to February 2012 using an  
55 Aerodyne HR-ToF-AMS for non-refractory PM<sub>1</sub> (PM with aerodynamic diameter less than 1 micron). In our  
56 previous studies, we found that photochemical oxidation during a haze episode and aqueous-phase reactions during  
57 two foggy periods both led to a high degree of oxygenation of organics due to aging in gas phase and/or aqueous  
58 phase with substantial SOA formation (Lee et al., 2013 and Li et al., 2013). In spring and summer, SOA, with  
59 abundant SVOOA, was more likely to form locally. The oxygen-to-carbon atomic ratio (O:C) and average carbon  
60 oxidation state ( $\overline{\text{OS}}_c$ ) peaked in the afternoon in spring and summer (Li et al., 2015). In autumn and winter, LVOOA  
61 dominated in SOA. The O:C ratio and  $\overline{\text{OS}}_c$  showed little diurnal variation. Huang et al. (2015) estimated the  
62 contents of organic sulfur compounds in Hong Kong in September 2011. They highlighted the importance of both  
63 aqueous-phase processing and regional influence for the formation of organic sulfur compounds. Closure analysis  
64 was performed between the PM hygroscopicity measured by a hygroscopic tandem differential mobility analyzer  
65 (HTDMA) and chemical composition measured by an HR-ToF-AMS and a constant growth factor of 1.18 for  
66 organics was found to be adequate for a good closure, given the dominant contribution of the very hygroscopic  
67 sulfate at this suburban site (Cheung et al., 2016; Yeung et al., 2014). Meng et al. (2014) found that the aerosol  
68 hygroscopic parameter ( $k$ ) decreased with an increasing organic-to-inorganic volume ratio. Furthermore, the  
69 concentration of cloud condensation nuclei (CCN) was found to be more sensitive to the mixing state and  
70 hygroscopicity of the particles at a high supersaturation (SS)=0.70% and a low SS=0.15%, respectively.

71 The above studies primarily focused on the analysis of campaign-average scenarios, without specifically  
72 looking at episodic events that occurred during the campaign. In the current study, we investigated the chemical  
73 transformation and size evolution of secondary aerosols in high particulate matter episodes across the four seasons.  
74 Specifically, we examined in detail the photochemical evolution in a particular episode in which local influences  
75 were dominant. Results from the current study reveal the rapid evolution of secondary aerosols and are relevant to  
76 other megacities with large precursor input and high photochemical activity.

## 77 **2. Experimental Section**

### 78 **2.1. Sampling Site and Measurements**

79 The sampling periods were from 25 April to 1 June 2011 (spring), from 1 September to 29 September 2011  
80 (summer), from 28 October to 15 December 2011 (autumn), and from 19 January to 1 March 2012 (winter). HR-

81 ToF-AMS measurements were conducted at the HKUST AQRS (22°20'N, 114°16'E). The HKUST supersite is  
82 located on the campus of HKUST, which sits on the hillside of Clear Water Bay on the east coast of Hong Kong that  
83 has relatively low population density. There is little local emission around the site. Two minor local sources include  
84 Clear Water Bay Road and a small student canteen. The Clear Water Bay Road is located outside of the campus and  
85 has mild traffic. The student canteen within 200m of the site, which operates only from 18:00LT (local time) until  
86 midnight. The HR-ToF-AMS operating procedure, data analysis and species determination have been discussed in  
87 Lee et al. (2013a), Li et al. (2015) and Huang et al. (2015). Briefly, the AMS was operated alternatively between the  
88 V+PToF combined mode and the W-mode for 5 min each. A collection efficiency of 0.5 was employed for  
89 measurements at this site, where the particles have overwhelmingly dominant sulfate content (Aiken et al., 2009; Li  
90 et al., 2013). Concentrations of methanesulfonic acid (MSA) and organosulfates (OS) were estimated by combining  
91 the V-mode data for total concentrations and the W-mode data for high-resolution mass spectral analysis for specific  
92 ions (Huang et al., 2015). Mass spectra of organic sulfur compounds were obtained from standards in laboratory  
93 experiments to support the W-mode data analysis (Huang et al., 2015). We further calculated the particle liquid  
94 water content (LWC) by applying E-AIM II (Clegg et al., 1998) to explore the effects of aqueous processing on PM<sub>1</sub>  
95 composition. Gaseous species (CO, CO<sub>2</sub>, SO<sub>2</sub>, NO, NO<sub>2</sub>, and O<sub>3</sub>) were measured with standard gas analyzers  
96 (Teledyne API). Volatile organic compounds (VOCs) were measured by gas chromatography (Synspec GC955).  
97 Meteorological parameters were measured by an automatic weather station mounted on a tower right next to the  
98 supersite. Particle hygroscopicity and size distribution measurements have previously been taken with a HR-ToF-  
99 AMS at this site (Cheung et al., 2015; Man et al., 2015; Meng et al., 2014; Yeung et al., 2014), and direct reference  
100 to the resulting publications will be made where necessary.

## 101 **2.2. Data analysis**

### 102 **2.2.1. Criteria for an episodic event**

103 The total non-refractory PM<sub>1</sub> (NR-PM<sub>1</sub>) concentration showed little seasonal variation, with monthly averages  
104 ranging from 14.3 to 15.9  $\mu\text{g m}^{-3}$  as reported by Li et al. (2015). In this work, we defined episodic events according  
105 to the following criteria: 1) lasting for at least 24 hours; 2) daily NR-PM<sub>1</sub> average mass concentration exceeding 15  
106  $\mu\text{g m}^{-3}$  (overall monthly averaged concentration); and 3) maximum concentration exceeding 30  $\mu\text{g m}^{-3}$ . According to  
107 these criteria, 10 episodic events were identified in the campaigns as shown in Figure S1.

### 108 **2.2.2. Source apportionment**

109 Following the results in Li et al. (2015), 72-hour backward air trajectory analysis and positive matrix  
110 factorization (PMF) analysis were performed. Briefly, the back trajectory analysis was run at an elevation of 300 m  
111 using the HYSPLIT-4.8 (Hybrid Single-Particle Lagrangian Integrated Trajectory) model developed by  
112 NOAA/ARL (U.S. National Oceanic and Air Administration/Air Resources Laboratory). We classified air masses  
113 affecting Hong Kong into long-, medium-, and short-range transport patterns for transport distances of 1000 km,  
114 between 500 and 1000 km, and less than 500 km, respectively (Su et al., 2015).

115 For PMF analysis, a four-factor solution with hydrocarbon-like organic aerosols (HOA), cooking organic  
116 aerosols (COA), SVOOA, and LVOOA was adopted as in Li et al. (2015). During episodic events, HOA and COA  
117 contributed insignificantly (less than 6% and 5% respectively) to total organic aerosol (OA). Since we are interested  
118 in SOA transformation, HOA and COA were combined into one POA factor in the following discussion.

### 119 **2.2.3. Size distribution**

120 Size distributions of aerosol species are obtained with the HR-ToF-AMS when a set of pre-selected  $m/z$  is  
121 scanned as a function of the particle time of flight. We focus on the size distribution analysis of sulfate and organics  
122 because of their overwhelming dominance in NR-PM<sub>1</sub>. The raw 10-min mass-size distributions of organics and  
123 sulfate during the episodic events were averaged over various time periods pertaining to the resolution (e.g. 24 hours,  
124 1 hour). The average size distributions were then fitted by the peak fitting tool Multipeak Fit V2 provided by Igor  
125 Pro (Wavemetrics) using two log-normal peaks. The peaks were chosen such that the fit residuals were minimized.  
126 The two fitted peaks of the size distributions will hereafter be referred to as the small particle mode and the large  
127 particle mode. Fitting examples can be found in Figure S2. We will focus on the most important fitting parameters:  
128 the particle mass-mode diameter (vacuum aerodynamic diameter,  $D_{va}$ ) indicating the shift in particle size and the  
129 integrated peak areas of the small particle mode and the large particle mode indicating the changes in mass  
130 concentrations of larger or smaller particles.

### 131 **2.2.4. Photochemical age**

132 The photochemical age is useful for studying the extent of photochemical processing in an air mass. One way to  
133 estimate the photochemical age ( $\Delta t$ ) is by the ratio of a less reactive hydrocarbon to a more reactive one (Kleinman,  
134 2003):



$$\Delta t = \frac{\ln\left(\frac{C_j}{C_i} * \frac{C_{i0}}{C_{j0}}\right)}{(k_i - k_j)[OH]} \quad (1)$$

136 in which  $C_i$  and  $C_j$  are concentrations of hydrocarbons  $i$  and  $j$  at time  $t$ , whereas  $C_{i0}$  and  $C_{j0}$  are concentrations of  
 137 hydrocarbons  $i$  and  $j$  at time 0. The symbols  $k_i$  and  $k_j$  are their respective rates of reaction with hydroxyl radicals  
 138 (OH). Hofzumahaus et al. (2009) reported a high average OH concentration of  $15 \times 10^6$  molecules  $\text{cm}^{-3}$  around noon  
 139 in the PRD region, much higher than model predictions. Zhou et al. (2014) used an OH concentration of  $5.2 \times 10^6$   
 140 molecules  $\text{cm}^{-3}$  in their calculation of photochemical age in the PRD region. Lacking definitive estimates, we used a  
 141 conservative OH concentration of  $1.5 \times 10^6$  molecule  $\text{cm}^{-3}$  (Hayes et al., 2013; Mao et al., 2009) for the discussion of  
 142 oxidation trends in this study. The ratio of benzene to toluene has been widely used (El Haddad et al., 2013) because  
 143 of their similar emission sources and significantly different rates of reaction with OH radicals ( $k_{\text{benzene-OH}} = 1.23 \times 10^7$   
 144  $\text{cm}^3 \text{molecule}^{-1} \text{s}^{-1}$ ;  $k_{\text{toluene-OH}} = 6.0 \times 10^{12} \text{cm}^3 \text{molecule}^{-1} \text{s}^{-1}$  at 298K) (Atkinson Roger, 2000). Because toluene  
 145 reacts more rapidly with OH radicals than does benzene, it is depleted more quickly, resulting in higher  
 146 benzene/toluene ratios in aged air masses. However, the photochemical age can deviate when fresh pollutants are  
 147 added to an aged air mass. Since fresh pollutants were insignificant after 10:00 (i.e. no significant peaks of benzene  
 148 and toluene after 10:00; see Figure S3), we set the start time at 10:00 for the discussion of photochemical aging.

### 149 **3. Results and Discussion**

#### 150 **3.1. Meteorological conditions and classification of episodes**

151 Table 1 summarizes the meteorological conditions,  $\text{PM}_{10}$  concentrations, and the estimated LWC in the 10 high  
 152 PM episodes. All of the episodes involved air masses that originated over East Asia from the north, northeast or  
 153 northwest of Hong Kong, and swept over part of the PRD region before reaching the site. Seven of the 10 episodes  
 154 (E1-E7) were characterized by medium-range trajectories and the other three (E8-E10) by long-range trajectories.  
 155 The individual trajectories are shown in Figure S4. E1 and E2 had much lower solar irradiance (IR) but higher LWC  
 156 than the other episodes, which distinguished them from the other medium-range transport episodes. Thus, E1 and E2  
 157 were categorized as episodes of the LWC type (medium-range transport with high LWC and low IR) and the other  
 158 medium-range transport episodes as episodes of the IR type (medium-range transport with high IR and low LWC).  
 159 Li et al. (2013) referred to E1 and E2 as foggy episodes, while Li et al. (2013) and Lee et al. (2013a) referred to E3

160 as a hazy episode. The long-range transport episodes might be less associated with the local site-specific conditions  
161 and were categorized as episodes of the LRT type.

162 High concentrations of PM can have a number of causes, including enhanced primary emissions (Ji et al., 2014),  
163 concentrating effects due to a decrease in the height of the planetary boundary layer (Petäjä et al., 2016), regional  
164 transport (Huang et al., 2009), as well as active secondary formation (Hayes et al., 2013). Local primary emissions  
165 were not very significant at this site, as can be seen from the low contribution of POA (less than 6%) throughout the  
166 whole campaign. As an indicator for primary PM, elemental carbon (EC) concentrations in PM<sub>2.5</sub> filter sampling at  
167 this site from March 2011 to February 2012 were also found to be low throughout the year ( $0.86 \pm 0.53$   
168  $\mu\text{g}/\text{m}^3$ ) (Huang et al., 2014b). Boundary layer dynamics on the high PM days can be a factor affecting PM  
169 concentration, but the effects were likely minimal as the highest concentration was usually observed during the day  
170 at higher mixing heights (Figure S5). Therefore, regional transport and active secondary formation would be the  
171 most probable causes for the episodic events of high PM concentrations at this suburban site. More detailed  
172 meteorological conditions with chemical characteristics in each episode can be found in Figure S5.

173 As is apparent from Table 1, the occurrence of different types of episodes exhibits a seasonal trend. LWC  
174 episodes occurred only in spring and LRT episodes only in winter, while IR episodes took place in spring, summer  
175 and autumn. This result is consistent with previous results (Huang et al., 2009) in that the frequency of high PM  
176 days in Hong Kong had a strong seasonal variation. In winter, the overwhelming northerly wind brings pollutants  
177 via long-range transport (Fang et al., 1999). In spring, foggy days with high PM levels are common due to the  
178 moisture-laden air masses coming in from the sea and aqueous-phase processing of particulate species (Li et al.,  
179 2013). In summer and autumn, however, hazy days are mainly due to high photochemical activities in this  
180 subtropical area, resulting in the formation of secondary aerosols (Hu et al., 2008; Zhou et al., 2014).

### 181 **3.2. Chemical characteristics of high PM episodes**

182 Figure 1 shows the chemical constituents of NR-PM<sub>1</sub> in the three types of episodes. It is apparent that sulfate  
183 dominated in all types of episodes. In Hong Kong, sulfate is largely regarded as a major regional pollutant with little  
184 spatial variability, as in the rest of the PRD (Hagler et al., 2006; LOUIE et al., 2005). Nitrate contributed less than 4%  
185 in LWC episodes and IR episodes, but more than 7% in LRT episodes. As LRT episodes occurred in wintertime,  
186 the higher nitrate concentration was likely driven by gas-particle partitioning of ammonium nitrate to the particle at

187 low temperatures (Seinfeld and Pandis, 2006). Using the PMF-resolved SVOOA and LVOOA as proxies for less-  
188 oxidized and more-oxidized SOA respectively (Zhang et al., 2011), more details of OA can be revealed. SVOOA  
189 had higher contributions in IR episodes, while LVOOA contributed roughly twice as much as SVOOA did in LRT  
190 episodes, because the air mass was already quite aged when reached the site. LVOOA and SVOOA made similar  
191 contributions in LWC episodes.

192 Figure 2 shows the diurnal variations of the NR-PM<sub>1</sub> species, PMF-resolved organic factors, as well as O<sub>x</sub>  
193 (O<sub>3</sub>+NO<sub>2</sub>) in these three types of episodes. SVOOA and LVOOA as well as O<sub>x</sub> increased during the day in IR  
194 episodes, with a time lag between SVOOA and LVOOA. A similar time lag was also observed between SVOOA  
195 and LVOOA in the Yangtze River Delta (YRD), another fast developing region of China (Huang et al., 2012). These  
196 delays may be the result of conversions from SVOOA to LVOOA in the afternoon. We explore such a possibility in  
197 Section 3.6. SVOOA and LVOOA both exhibit flat diurnal patterns in LWC episodes and LRT episodes.

198 Elemental analysis of OA (ratios of H:C, O:C, N:C, S:C and OM:OC) from the high resolution mass spectra  
199 provides useful information to assess OA evolution. Recently, Canagaratna et al. (2015) used an updated (Improved-  
200 Ambient) method to estimate O:C and H:C ratios, and reported 27% higher O:C ratios and 11% higher H:C ratios  
201 than those estimated using the original (Aiken-Ambient) method. Recalculating the elemental ratios for the  
202 September dataset using the updated method shows little difference from those obtained by simply applying the  
203 respective factors of 1.27 and 1.11 to the O:C and H:C ratios (Figure S6). Hence, the O:C and H:C ratios in this  
204 study were corrected by factors of 1.27 and 1.11, respectively, with Aiken-Ambient values reported in our previous  
205 studies. In the Van Krevelen diagram (Heald et al., 2010; Ng et al., 2011) shown in Figure 3a, data points for LWC  
206 episodes (blue) fall into a lower O:C region than do the data points for IR (red) and LRT episodes (green).

207 Although aqueous-phase processing might generate highly oxygenated organic compounds (Li et al.,  
208 2016; Mazzoleni et al., 2010; Zhao et al., 2013), sampling by the AMS was only limited to interstitial  
209 particles and a portion of very small fog droplets after drying. This can also lead to O:C ratios lower than  
210 those in IR periods when most of the photochemically oxidized OA were effectively sampled. Even though  
211 data points for IR episodes and LRT episodes have similar slopes and intercepts in the Van Krevelen diagram, data  
212 points for IR episodes had a much wider spread. These trends are also reflected in the diurnal patterns of carbon  
213 oxidation state ( $\overline{\text{OS}}_c \approx 2 \times \text{O:C-H:C}$ ) (Kroll et al., 2011) in Figure 3b. The  $\overline{\text{OS}}_c$  diurnal pattern in LRT episodes was  
214 relatively flat, suggesting that oxidized organics were mostly transported to the site with minor in-situ oxidation.

215 The  $\overline{OS}_c$  in IR episodes gradually increased from 09:00 until 15:00. Similar trends were observed for  $O_x$ , LVOOA  
216 and to a less extent, SVOOA. With all these combined, we believe that the local photochemical processing of OA  
217 was more likely at play in IR episodes than the long-range transport of processed aerosols.

218

### 219 **3.3. Size distributions of sulfate and organics**

220 Figure 4 shows the peak fitting results of the type-averaged size distributions of organics and sulfate mass. The  
221 mass-mode diameters ( $D_{va}$ ) for both the small and large modes of organics and sulfate did not differ considerably  
222 across the episode types (differing by less than 5%). Within each type of episode, sulfate had a smaller fraction of  
223 small particle mode than organics did, indicating that sulfate was relatively aged while organics received  
224 contributions from local fresh emissions. LWC episodes received the largest contribution from small mode sulfate  
225 because of some local influences whereas LRT episodes received the smallest contribution with relatively little local  
226 activities. The oxidation mechanisms, however, might be different. Aqueous phase oxidation may dominate in  
227 LWC episodes while photochemical oxidation may dominate in IR episodes.

228 Various studies have analyzed the particle mixing state using single-particle instruments such as the aerosol time-  
229 of-flight mass spectrometer (Healy et al., 2013, 2014; Yang et al., 2012) and the single-particle aerosol mass  
230 spectrometer (Wang et al., 2015). Particle mixing state can also be inferred from particle size information obtained  
231 with the AMS. If the organics and sulfate are internally mixed (i.e. they exist in the same particle), their diameters  
232 should be strongly correlated with each other and their size should grow at a similar rate. The observed strong  
233 correlation and slope of unity (correlated in time and size) suggest that these species are likely internally mixed,  
234 although we cannot completely exclude the possibility of external mixing. On the other hand, if the mode diameters  
235 of sulfate and organics did not change coherently and exhibit a strong correlation with a slope close to unity, these  
236 particles were more likely externally mixed. Bahreini et al. (2003) have used such correlations in size to indicate the  
237 mixing states of species. In our study, the large mode diameters of organics and sulfate were strongly correlated  
238 (Pearson's R value equals 0.7) with a slope close to unity in LWC episodes (Figure 5), suggesting that organics and  
239 sulfate were likely internally mixed in the large particles. However, these conditions of correlation and slope are  
240 necessary but not sufficient evidence for internal mixing. This internal mixing may occur during the process of local  
241 aqueous oxidation. In IR episodes, during which local photochemical oxidation may have a more obvious influence,

242 larger particles do not mix well internally (poor correlation between the large mode diameters of organics and  
243 sulfate with  $R_{pr} = 0.2$ ). As discussed in Section 3.2, in IR episodes, organics showed a clear noontime peak  
244 associated with local photochemical activities while sulfate was still mainly a regional pollutant. As a result, large  
245 particles of organics and sulfates were very likely to have been externally mixed during IR episodes. A good  
246 correlation ( $R_{pr} = 0.7$ ) with the slope deviating substantially from unity (slope = 0.5) was observed in LRT episodes.  
247 As long-range transport was the dominant process causing high PM levels during LRT episodes, organics and  
248 sulfate would have been brought to the site together, so their large mode diameters tend to be strongly correlated.  
249 However, they may have different origins and may also have undergone different aging processes during the course  
250 of long-range transport, and thus their mode diameters would be different. The correlations between the small mode  
251 diameters of organics and sulfate were notably weaker, with  $R_{pr}=0.5$  in LWC episodes,  $R_{pr}=0.2$  in IR episodes, and  
252  $R_{pr}=0.2$  in LRT episodes, suggesting that freshly formed small particles mixed externally.

253 As discussed earlier, there may be some local atmospheric processing of aerosols in LWC and IR episodes but not  
254 in LRT episodes. Therefore, we further explored the mechanisms underlying the atmospheric processing of LWC  
255 and IR episodes based on the size variations before and during episodic events. Figure 6 shows the particle mass  
256 mode diameters and areas (concentrations) in the LWC and IR types of episodes. We obtained the percentage  
257 changes in mode diameters by comparing the smallest diameter before the episode and the largest diameter during  
258 the episode for each episode. These percentages in each episode was then averaged to obtain the percentage changes  
259 for each episode type. The results show that the changes in mode diameter were small in the LWC episodes: -2.5%  
260 for small mode organics, +8.1% for large mode organics, +1.6% for small mode sulfate, and -3% for large mode  
261 sulfate. In contrast, the changes in mode diameters changes were much more drastic in the IR episodes: +51.3% for  
262 small mode organics, +40.5% for large mode organics, +45.4% for small mode sulfate, and +35.9% for large mode  
263 sulfate. Furthermore, particle size usually increased more rapidly before the IR episodes (shaded in blue in Figure 6)  
264 than during the episodes (shaded in orange). With fewer pre-existing particles before the episodes, particle growth  
265 likely via condensation and reactive uptake of semi-volatile components was more rapid than during the episodes.  
266 The number concentration is discussed in detail in SI.

### 267 **3.4. Local photochemical formation and evolution of PM: A case study**

#### 268 **3.4.1. Time series of species during the local photochemical episode**

269 Because of the high frequency of occurrence of IR episodes, we chose one IR episode (E4) to examine the  
270 evolution of the aerosols with photochemical oxidation. This particular episode (E4) was under the influence of a  
271 clear land-sea breeze pattern with weak winds (Figure 7), a typical meteorological phenomenon that affects air  
272 pollution dynamics at this coastal city (Lee et al., 2013a). As can be seen from Figure 7, the maximum wind speed  
273 was less than  $2 \text{ m s}^{-1}$  while the average wind speed was approximately  $0.5 \text{ m s}^{-1}$ . The wind direction changed from  
274 northerly to easterly between 06:00 and 10:00 and remained easterly until 20:00, when it changed clockwise from  
275 easterly back to northerly. Under such conditions, local photochemical activities can lead to effective production and  
276 accumulation of air pollutants. Time series of organics, sulfate, ammonium, nitrate, MSA, OS, PMF-resolved  
277 organic factors, some gaseous species, as well as meteorological parameters were analyzed. Most NR-PM<sub>1</sub> species  
278 showed clear diurnal variations. Figure 7 shows that organics increased from a roughly constant concentration of  $10$   
279  $\mu\text{g m}^{-3}$  at night until 09:00 to its highest concentration of  $16.6 \mu\text{g m}^{-3}$  at 13:00, while sulfate showed a mild increase  
280 at 06:00 and then a sharp increase at 10:30 to reach its highest concentration of  $17.4 \mu\text{g m}^{-3}$  at 16:00. They were  
281 overall consistent with the increasing trend of irradiance, an indicator of photochemical activities, in the afternoon.  
282 Nitrate concentration was high ( $2.5 \mu\text{g m}^{-3}$ ) in the morning and started to decrease from 12:30 onwards to reach  $0.3$   
283  $\mu\text{g m}^{-3}$  by 16:00, likely attributable to vertical dilution due to a rise in the height of the planetary boundary layer, or  
284 alternatively evaporation of ammonium nitrate at higher temperatures and lower RH values (Seinfeld and Pandis,  
285 2006). Wind direction started to change at 20:00, when all the NR-PM<sub>1</sub> species were at their lowest concentrations.  
286 POA concentration increased from  $2.5 \mu\text{g m}^{-3}$  at 00:00 to about  $5 \mu\text{g m}^{-3}$  at 06:00, which might be due to the  
287 lowering of the planetary boundary layer. Conversely, expansion of the boundary layer early in the morning could  
288 help disperse the POA. The increase in LVOOA lagged behind that in SVOOA. Starting from 06:00, SVOOA  
289 concentration increased rapidly and peaked at approximately 13:00, coinciding with the IR peak, possibly due to  
290 SOA formation. LVOOA gradually increased from 12:00 and peaked at 14:00, similar to sulfate. The time lag  
291 suggests that some conversion from less-oxidized to more-oxidized SOA might have occurred in the afternoon.  
292 Evaporation at the elevated temperature of  $30^{\circ}\text{C}$  throughout the afternoon might also have led to the decrease in  
293 SVOOA, as with nitrate. The diurnal variation of MSA shows a noontime peak, consistent with the trend of  
294 irradiance. In contrast, OS did not show a clear noontime peak, since OS at this site were likely affected by inland  
295 transportation (Huang et al., 2015).

#### 296 3.4.2. Changes in size distribution

297 As shown Figure 8, before 06:00, the size distributions of sulfate and organics were both dominated by a mass  
298 mode diameter of 500 to 600 nm. During 06:00-09:00, a shoulder at 200 nm appeared in the size distribution of  
299 sulfate and in that of organics, indicating some fresh sulfate and organics were formed or emitted (possibly POA).  
300 As photochemical reactions proceeded (09:00-18:00), the shoulder of  $D_{va}$  at 200 nm became weaker and the size  
301 distributions shifted to the larger end. It should be noted that during the whole aging process, the size distributions of  
302 organics were broader than those of sulfate since organics were a mixture of numerous constituents from different  
303 primary sources and reaction products formed via different atmospheric processes. The shifts in size distribution  
304 suggest that secondary aerosol particles with sulfate and organics aged gradually and grew into larger particles.

### 305 3.4.3. Photochemical production of secondary species

306 We examine the daytime photochemical activity during E4 by looking at the  $\text{SO}_2$  oxidation and changes in the  
307 degree of oxygenation of particulate organics. The sulfur oxidation ratio (SOR) has been used to evaluate the extent  
308 of atmospheric oxidation of  $\text{SO}_2$  to sulfate (Squizzato et al., 2013; Wang et al., 2005). Figure 9c shows the increase  
309 in SOR from 0.2 at 9:00 to 0.7 at 18:00, indicating an efficient conversion from  $\text{SO}_2$  to sulfate during daytime in this  
310 episode. Figure 9b shows that the  $\overline{\text{OS}}_c$  increased sharply near 11:00.  $\overline{\text{OS}}_c$  was high after 18:00 because most of the  
311 organics in PM had been converted to highly oxidized organic compounds during the aging process. Indeed, during  
312 this period, LVOOA was the dominant OA component (Figure 7). The increases in SOR and  $\overline{\text{OS}}_c$  coincided with  
313 the increase in the ratio of benzene to toluene (Figure 9). The oxidation of sulfur species and organic species reflects  
314 efficient oxidation during this photochemical episode.

315 To semi-quantitatively evaluate the efficiency of SOA and sulfate formation, the changes in  $\text{SOA}/\Delta\text{CO}$ ,  
316  $\text{MSA}/\Delta\text{CO}$ , and  $\text{sulfate}/\Delta\text{CO}$  are plotted in Figure 10 as a function of photochemical age from 10:00 to 18:00.  $\Delta\text{CO}$ ,  
317 defined as the measured CO concentration minus the minimum CO concentration (see Figure 7 for the time series of  
318 CO), is assumed to be a conservative tracer of urban combustion emissions. The perturbations of CO concentration  
319 by photochemical formation from VOC or destruction by OH radicals were thought to be negligible over such a  
320 short timescale (less than eight hours) (Griffin et al., 2007). Normalization of species concentrations to the  $\Delta\text{CO}$   
321 concentration is expected to reduce the effect of dilution (Hayes et al., 2013; Zhou et al., 2014).

322 From 10:00 to 18:00,  $\text{sulfate}/\Delta\text{CO}$  increased by a factor of 7-8 as photochemical activity increased on a  
323 timescale of approximately 6 h, with a formation rate (indicated by the slope of  $\text{species}/\Delta\text{CO}$  vs. photochemical age)  
324 of approximately  $48 \mu\text{g m}^{-3} \text{ppm}^{-1} \text{h}^{-1}$ .  $\text{MSA}/\Delta\text{CO}$  also increased by a factor of approximately 3 at a rate of  $0.05 \mu\text{g}$

325  $\text{m}^{-3} \text{ppm}^{-1} \text{h}^{-1}$  during photochemical aging. The good correlation of MSA production with the photochemical age  
326 suggests that MSA originated from the reaction of gaseous dimethyl sulfide with OH radicals (Barnes et al., 2006).  
327 For comparison, Bardouki et al. (2003) also found that MSA and OH radicals covaried over the northeastern coast of  
328 Crete. As shown in Figure 10c, SOA/ $\Delta\text{CO}$  increased by approximately a factor of 2 with the slope of  $7.2 \mu\text{g m}^{-3}$   
329  $\text{ppm}^{-1} \text{h}^{-1}$  ( $8.07 \mu\text{g sm}^{-3} \text{ppm}^{-1} \text{h}^{-1}$ ). A shallower slope (approximately  $4.0$  to  $4.5 \mu\text{g sm}^{-3} \text{ppm}^{-1} \text{h}^{-1}$ ) was observed in  
330 Pasadena, California from May to June (Hayes et al., 2013) while a similar slope ( $6.18 \mu\text{g m}^{-3} \text{ppm}^{-1} \text{h}^{-1}$ ) was  
331 observed in a previous study in Hong Kong in August (Zhou et al., 2014). This indicates that the SOA production in  
332 Hong Kong during the local in situ photochemical oxidation in summer is high.

333 More interestingly, SVOOA/ $\Delta\text{CO}$  increased during the first three hours but decreased slightly after 13:00, even  
334 as photochemical age increased. In contrast, LVOOA/ $\Delta\text{CO}$  increased steadily throughout the whole stage. After  
335 photochemical processing for 6 h, LVOOA/ $\Delta\text{CO}$  increased by approximately a factor of 20, from  $2.3 \mu\text{g m}^{-3} \text{ppm}^{-1}$   
336 to  $49.4 \mu\text{g m}^{-3} \text{ppm}^{-1}$ . Even though both SVOOA/ $\Delta\text{CO}$  and LVOOA/ $\Delta\text{CO}$  increased in the first stage, they did so at  
337 slightly different rates, where SVOOA/ $\Delta\text{CO}$  increased faster than LVOOA/ $\Delta\text{CO}$ . This suggests that the production  
338 of SVOOA was more efficient than that of LVOOA in the first stage. However, in the later stage of SOA formation,  
339 the net productions of SVOOA were negative, which indicates that SVOOA may have photochemically converted to  
340 LVOOA. As discussed earlier, the input of POA and VOC was limited to the early morning in our study. SVOOA  
341 was consumed more quickly to form LVOOA than was replenished through further production in the late afternoon.  
342 The situation where limited precursors exist to replenish fresh SOA (even under strong photochemical activity)  
343 might also occur in other non-urban atmospheric environments, and thus may have an implication for OA  
344 transformation in general.

#### 345 **3.4.4. Mass spectral evolution**

346 Figure 11a shows the evolving organic mass spectra during E4 (corresponding to the period of photochemical  
347 aging). Eight spectra at one-hour intervals from 10:00 to 18:00 are shown from top to bottom. Two changes in the  
348 mass spectra with photochemical processes were apparent: 1) decreases in the signal intensities of relatively high  
349  $m/z$  ions (e.g.,  $m/z$  55, 57, 67, 69, etc.), which indicates greater fragmentation (C-C bond cleavage) with  
350 photochemical oxidation; and 2) increases in the mass concentrations of ions having  $m/z$  values of 28 (mainly  $\text{CO}^+$ )  
351 and 44 (mainly  $\text{CO}_2^+$ ), which presumably come from aldehyde, ketone and carboxylic acid (Ng et al., 2011). These  
352 changes are also reflected in the relative intensity changes of hydrocarbon-like and oxygen-containing ions such as



353  $C_4H_7^+$ ,  $C_2H_3O^+$  and  $CO_2^+$  (Figure 11b, c). The fractions of tracers of primary organic aerosols  $C_3H_7^+$  (m/z 43),  $C_4H_7^+$   
354 (m/z 55) and  $C_4H_9^+$  (m/z 57) (Lambe et al., 2012) decreased. On the other hand, ion fractions of  $C_2H_3O^+$  (m/z 43),  
355  $C_3H_3O^+$  (m/z 55) and  $C_3H_5O^+$  (m/z 57) increased until 13:00 (corresponding to the peak of SVOOA), followed by  
356 the decrease of these moderately oxygenated ions. These ions are predominantly from non-acid oxygenates, and are  
357 usually associated with less-oxidized SOA. However, The most oxidized ions,  $CO_2^+$  (m/z 44), which is thought to be  
358 the marker of more-oxidized SOA, increased continuously. As a result, the mass spectra, which were initially  
359 SVOOA-like, evolved to become LVOOA-like with increasing photochemical age (Figure 11d). Overall, this  
360 spectral analysis indicates increasingly oxidized organics, as long carbon chains became more functionalized and  
361 fragmented after extensive oxidation (Alfarra et al., 2012; Kroll et al., 2009). Such an observation implies efficient  
362 transformation of OA within a few hours of photochemical aging, a timescale that could be relevant to chemical  
363 transport models concerning SOA formation.

#### 364 4. Conclusion

365 High-resolution HR-ToF-AMS measurements were taken during four one-month campaigns in suburban Hong  
366 Kong to illustrate the evolution of high PM episodic events across the seasons. Three types of episodes, medium-  
367 range transport with high particle liquid water content (LWC episodes), medium-range transport with high solar  
368 irradiance (IR episodes), and long-range transport (LRT episodes), were captured based on synoptic meteorological  
369 conditions. Which type of episode occurred depended on the season, with LWC episodes occurring only in spring  
370 and LRT episodes only in winter, while IR episodes took place throughout the year except in winter. Sulfate was the  
371 major constituent of NR-PM<sub>1</sub> during all episodic events. The contribution of secondary organic species, including  
372 SVOOA and LVOOA, varied across episode types, with more SVOOA in the IR episodes and more LVOOA in the  
373 LRT episodes. Unlike in the other two types of episodes, in IR episodes organics experienced the most dramatic  
374 diurnal variation, with a time lag between SVOOA and LVOOA. This variation was associated with Ox, indicating  
375 the conversions from less-oxidized to more-oxidized SOA under photochemical oxidation. Elemental analysis  
376 involving the Van Krevelen diagram and carbon oxidation state ( $\overline{OS}_c \approx 2 \times O:C-H:C$ ) further showed that organics in  
377 IR were gradually oxidized.

378 Fitted mass-mode diameters for both the small and the large mode of organics remained roughly constant across  
379 episode types, while sulfate had a constant small mode diameter in all three types of episodes but a slightly  
380 increased large mode diameter in IR episodes. The fraction of small particles decreased from LWC episodes to IR

381 episodes then to LRT episodes, suggesting that aerosols from long-range transport were more aged and dominated  
382 by large particles while episodes under a greater influence of local processes had a higher proportion of fresher  
383 small particles. Large particles mixed internally only in LWC episodes, and were more likely to mix externally in IR  
384 and LRT episodes. Freshly formed small particles mixed externally in all types of episodes. In IR episodes, aerosols  
385 underwent an obvious size increase, while in LWC episodes, the size increase was much less drastic.

386 Because of the high frequency of IR episodes, we picked one particular IR episode featuring land-sea breeze to  
387 examine in detail the evolution of aerosol components. Photochemical aging led to mode size shifting for sulfate and  
388 organics, indicating particle growth. Increases in the sulfur oxidation ratio and carbon oxidation state were also  
389 observed as the aerosols became more aged, which indicates that secondary inorganic species sulfate and SOA were  
390 very efficiently produced within six hours of photochemical aging. In the earlier stage of aging, “less-oxidized”  
391 SOA—SVOOA—was formed at a higher rate than “more-oxidized” SOA—LVOOA. SVOOA clearly transformed  
392 to LVOOA at the later stage of photochemical aging, resulting in a 20-fold increase in LVOOA. This conversion  
393 was further supported by mass spectral analysis, which showed an increase in the most oxidized ion ( $\text{CO}_2^+$ ) and  
394 decreases in moderately oxidized ones ( $\text{C}_2\text{H}_3\text{O}^+$ ,  $\text{C}_3\text{H}_3\text{O}^+$  and  $\text{C}_3\text{H}_5\text{O}^+$ ). With real-time size-resolved chemical  
395 composition data, we demonstrated that aerosol components can transform very efficiently in just a few hours, a  
396 process that is essential in understanding the dynamic nature of aerosol evolution during episodes with high PM  
397 concentrations.

### 398 **Acknowledgements**

399 This work was supported by the Environmental Conservation Fund of Hong Kong (project number ECWW09EG04)  
400 and the Research Grants Council of the Hong Kong Special Administrative Region, China (General Research Fund  
401 600413). Y.J. Li gratefully acknowledges the support from the Start-up Research Grant (SRG2015-00052-FST) of  
402 the University of Macau. The grant from the HKUST Asian Future Leaders Scholarship Program (AFLSP) is also  
403 gratefully acknowledged.

404

405

406

407

408

409

410

411 **References**

412 Aiken, A. C., Salcedo, D., Cubison, M. J., Huffman, J. A., DeCarlo, P. F., Ulbrich, I. M., Docherty, K. S., Sueper,  
413 D., Kimmel, J. R., Worsnop, D. R., Trimborn, A., Northway, M., Stone, E. A., Schauer, J. J., Volkamer, R. M.,  
414 Fortner, E., de Foy, B., Wang, J., Laskin, A., Shutthanandan, V., Zheng, J., Zhang, R., Gaffney, J., Marley, N. A.,  
415 Paredes-Miranda, G., Arnott, W. P., Molina, L. T., Sosa, G. and Jimenez, J. L.: Mexico City aerosol analysis during  
416 MILAGRO using high resolution aerosol mass spectrometry at the urban supersite (T0) – Part 1: Fine particle  
417 composition and organic source apportionment, *Atmos. Chem. Phys.*, 9(17), 6633–6653, doi:10.5194/acp-9-6633-  
418 2009, 2009.

419 Alfarra, M. R., Hamilton, J. F., Wyche, K. P., Good, N., Ward, M. W., Carr, T., Barley, M. H., Monks, P. S., Jenkin,  
420 M. E., Lewis, A. C. and McFiggans, G. B.: The effect of photochemical ageing and initial precursor concentration  
421 on the composition and hygroscopic properties of  $\beta$ -caryophyllene secondary organic aerosol, *Atmos. Chem. Phys.*,  
422 12(14), 6417–6436, doi:10.5194/acp-12-6417-2012, 2012.

423 Atkinson Roger, J. A.: Atmospheric degradation of volatile methyl-silicon compounds, *Environ. Sci. Technol.*,  
424 34(10), 1970–1976, doi:10.1021/es9910053, 2000.

425 Bardouki, H., Berresheim, H., Vrekoussis, M., Sciare, J., Kouvarakis, G., Oikonomou, K., Schneider, J. and  
426 Mihalopoulos, N.: Gaseous (DMS, MSA, SO<sub>2</sub>, H<sub>2</sub>SO<sub>4</sub> and DMSO) and particulate (sulfate and methanesulfonate)  
427 sulfur species over the northeastern coast of Crete, *Atmos. Chem. Phys.*, 3(5), 1871–1886, doi:10.5194/acp-3-1871-  
428 2003, 2003.

429 Barnes, I., Hjorth, J. and Mihalopoulos, N.: Dimethyl sulfide and dimethyl sulfoxide and their oxidation in the  
430 atmosphere, *Chem. Rev.*, 106(3), 940–975, doi:10.1021/cr020529+, 2006.

431 Canagaratna, M. R., Jimenez, J. L., Kroll, J. H., Chen, Q., Kessler, S. H., Massoli, P., Hildebrandt Ruiz, L., Fortner,  
432 E., Williams, L. R., Wilson, K. R., Surratt, J. D., Donahue, N. M., Jayne, J. T. and Worsnop, D. R.: Elemental ratio  
433 measurements of organic compounds using aerosol mass spectrometry: characterization, improved calibration, and  
434 implications, *Atmos. Chem. Phys.*, 15(1), 253–272, doi:10.5194/acp-15-253-2015, 2015.

435 Cheung, H. H. Y., Yeung, M. C., Li, Y. J., Lee, B. P. and Chan, C. K.: Relative Humidity-Dependent HTDMA  
436 Measurements of Ambient Aerosols at the HKUST Supersite in Hong Kong, China, *Aerosol Sci. Technol.*, 49(8),  
437 643–654, doi:10.1080/02786826.2015.1058482, 2015.

438 Cheung, H. H. Y., Tan, H., Xu, H., Li, F., Wu, C., Yu, J. Z. and Chan, C. K.: Measurements of non-volatile aerosols  
439 with a VTDMA and their correlations with carbonaceous aerosols in Guangzhou, China, *Atmos. Chem. Phys.*,  
440 16(13), 8431–8446, doi:10.5194/acp-16-8431-2016, 2016.

441 Clegg, S. L., Brimblecombe, P. and Wexler, A. S.: Thermodynamic Model of the System  $\text{H}^+ - \text{NH}_4^+ - \text{Na}^+ - \text{SO}_4^{2-} - \text{NO}_3^- - \text{Cl}^- - \text{H}_2\text{O}$  at 298.15 K, *J. Phys. Chem. A*, 102(12), 2155–2171, doi:10.1021/jp973043j, 1998.

443 Decarlo, P. F., Kimmel, J. R., Trimborn, A., Northway, M. J., Jayne, J. T., Aiken, A. C., Gonin, M., Fuhrer, K.,  
444 Horvath, T., Docherty, K. S., Worsnop, D. R. and Jimenez, J. L.: Field-Deployable, High-Resolution, Time-of-  
445 Flight Aerosol Mass Spectrometer, *Anal. Chem.*, 78(24), 8281–8289, doi:8410.1029/2001JD001213. Analytical,  
446 2006.

447 DeCarlo, P. F., Dunlea, E. J., Kimmel, J. R., Aiken, a. C., Sueper, D., Crounse, J., Wennberg, P. O., Emmons, L.,  
448 Shinozuka, Y., Clarke, a., Zhou, J., Tomlinson, J., Collins, D. R., Knapp, D., Weinheimer, A. J., Montzka, D. D.,  
449 Campos, T. and Jimenez, J. L.: Fast airborne aerosol size and chemistry measurements above Mexico City and  
450 Central Mexico during the MILAGRO campaign, *Atmos. Chem. Phys.*, 8(14), 4027–4048, doi:10.5194/acp-8-4027-  
451 2008, 2008.

452 Decarlo, P. F., Ulbrich, I. M., Crounse, J., De Foy, B., Dunlea, E. J., Aiken, a. C., Knapp, D., Weinheimer, A. J.,

453 Campos, T., Wennberg, P. O. and Jimenez, J. L.: Investigation of the sources and processing of organic aerosol over  
454 the Central Mexican Plateau from aircraft measurements during MILAGRO, *Atmos. Chem. Phys.*, 10(12), 5257–  
455 5280, doi:10.5194/acp-10-5257-2010, 2010.

456 Fang, M., Zheng, M., Wang, F., Chim, K. and Kot, S.: The long-range transport of aerosols from northern China to  
457 Hong Kong - a multi-technique study, *Atmos. Environ.*, 33(11), 1803–1817 [online] Available from:  
458 <http://repository.ust.hk/ir/Record/1783.1-28286> (Accessed 9 November 2015), 1999.

459 Griffin, R. J., Chen, J., Carmody, K., Vutukuru, S. and Dabdub, D.: Contribution of gas phase oxidation of volatile  
460 organic compounds to atmospheric carbon monoxide levels in two areas of the United States, *J. Geophys. Res.*,  
461 112(D10), D10S17, doi:10.1029/2006JD007602, 2007.

462 El Haddad, I., D'Anna, B., Temime-Roussel, B., Nicolas, M., Boreave, a., Favez, O., Voisin, D., Sciare, J., George,  
463 C., Jaffrezo, J.-L., Wortham, H. and Marchand, N.: Towards a better understanding of the origins, chemical  
464 composition and aging of oxygenated organic aerosols: case study of a Mediterranean industrialized environment,  
465 Marseille, *Atmos. Chem. Phys.*, 13(15), 7875–7894, doi:10.5194/acp-13-7875-2013, 2013.

466 Hagler, G. S. W., Bergin, M. H., Salmon, L. G., Yu, J. Z., Wan, E. C. H., Zheng, M., Zeng, L. M., Kiang, C. S.,  
467 Zhang, Y. H., Lau, A. K. H. and Schauer, J. J.: Source areas and chemical composition of fine particulate matter in  
468 the Pearl River Delta region of China, *Atmos. Environ.*, 40(20), 3802–3815, doi:10.1016/j.atmosenv.2006.02.032,  
469 2006.

470 Hayes, P. L., Ortega, a. M., Cubison, M. J., Froyd, K. D., Zhao, Y., Cliff, S. S., Hu, W. W., Toohey, D. W., Flynn, J.  
471 H., Lefter, B. L., Grossberg, N., Alvarez, S., Rappenglück, B., Taylor, J. W., Allan, J. D., Holloway, J. S., Gilman, J.  
472 B., Kuster, W. C., De Gouw, J. a., Massoli, P., Zhang, X., Liu, J., Weber, R. J., Corrigan, a. L., Russell, L. M.,  
473 Isaacman, G., Worton, D. R., Kreisberg, N. M., Goldstein, a. H., Thalman, R., Waxman, E. M., Volkamer, R., Lin,  
474 Y. H., Surratt, J. D., Kleindienst, T. E., Offenberg, J. H., Dusanter, S., Griffith, S., Stevens, P. S., Brioude, J.,  
475 Angevine, W. M. and Jimenez, J. L.: Organic aerosol composition and sources in Pasadena, California, during the  
476 2010 CalNex campaign, *J. Geophys. Res. Atmos.*, 118(16), 9233–9257, doi:10.1002/jgrd.50530, 2013.

477 Heald, C. L., Kroll, J. H., Jimenez, J. L., Docherty, K. S., Decarlo, P. F., Aiken, a. C., Chen, Q., Martin, S. T.,  
478 Farmer, D. K. and Artaxo, P.: A simplified description of the evolution of organic aerosol composition in the  
479 atmosphere, *Geophys. Res. Lett.*, 37(8), doi:10.1029/2010GL042737, 2010.

480 Ho, K. ., Lee, S. ., Chan, C. K., Yu, J. C., Chow, J. C. and Yao, X. .: Characterization of chemical species in PM<sub>2.5</sub>  
481 and PM<sub>10</sub> aerosols in Hong Kong, *Atmos. Environ.*, 37(1), 31–39, doi:10.1016/S1352-2310(02)00804-X, 2003.

482 Hofzumahaus, A., Rohrer, F., Lu, K., Bohn, B., Brauers, T., Chang, C.-C., Fuchs, H., Holland, F., Kita, K., Kondo,  
483 Y., Li, X., Lou, S., Shao, M., Zeng, L., Wahner, A. and Zhang, Y.: Amplified trace gas removal in the troposphere.,  
484 *Science*, 324(5935), 1702–1704, doi:10.1126/science.1164566, 2009.

485 Hu, D., Bian, Q., Li, T. W. Y., Lau, A. K. H. and Yu, J. Z.: Contributions of isoprene, monoterpenes,  $\beta$ -  
486 caryophyllene, and toluene to secondary organic aerosols in Hong Kong during the summer of 2006, *J. Geophys.*  
487 *Res. Atmos.*, 113(22), 1–14, doi:10.1029/2008JD010437, 2008.

488 Huang, D. D., Li, Y. J., Lee, B. P. and Chan, C. K.: Analysis of Organic Sulfur Compounds in Atmospheric  
489 Aerosols at the HKUST Supersite in Hong Kong Using HR-ToF-AMS, *Environ. Sci. Technol.*, 150305134049007,  
490 doi:10.1021/es5056269, 2015.

491 Huang, R.-J., Zhang, Y., Bozzetti, C., Ho, K.-F., Cao, J.-J., Han, Y., Daellenbach, K. R., Slowik, J. G., Platt, S. M.,  
492 Canonaco, F., Zotter, P., Wolf, R., Pieber, S. M., Bruns, E. a., Crippa, M., Ciarelli, G., Piazzalunga, A.,  
493 Schwikowski, M., Abbaszade, G., Schnelle-Kreis, J., Zimmermann, R., An, Z., Szidat, S., Baltensperger, U.,  
494 Haddad, I. El and Prévôt, A. S. H.: High secondary aerosol contribution to particulate pollution during haze events  
495 in China, *Nature*, doi:10.1038/nature13774, 2014a.

496 Huang, X.-F. F., Yu, J. Z., Yuan, Z. B., Lau, A. K. H. H. and Louie, P. K. K. K.: Source analysis of high particulate  
497 matter days in Hong Kong, *Atmos. Environ.*, 43(6), 1196–1203, doi:10.1016/j.atmosenv.2008.10.013, 2009.

498 Huang, X. F., He, L. Y., Xue, L., Sun, T. L., Zeng, L. W., Gong, Z. H., Hu, M. and Zhu, T.: Highly time-resolved  
499 chemical characterization of atmospheric fine particles during 2010 Shanghai World Expo, *Atmos. Chem. Phys.*,  
500 12(11), 4897–4907, doi:10.5194/acp-12-4897-2012, 2012.

501 Huang, X. H. H., Bian, Q., Ng, W. M., Louie, P. K. K. and Yu, J. Z.: Characterization of PM<sub>2.5</sub> major components  
502 and source investigation in suburban Hong Kong: A one year monitoring study, *Aerosol Air Qual. Res.*, 14(1), 237–  
503 250, doi:10.4209/aaqr.2013.01.0020, 2014b.

504 Ji, D., Li, L., Wang, Y., Zhang, J., Cheng, M., Sun, Y., Liu, Z., Wang, L., Tang, G., Hu, B., Chao, N., Wen, T. and  
505 Miao, H.: The heaviest particulate air-pollution episodes occurred in northern China in January, 2013: Insights  
506 gained from observation, *Atmos. Environ.*, 92, 546–556, doi:10.1016/j.atmosenv.2014.04.048, 2014.

507 Jimenez, J. L., Canagaratna, M. R., Donahue, N. M., Prevot, a S. H., Zhang, Q., Kroll, J. H., DeCarlo, P. F., Allan, J.  
508 D., Coe, H., Ng, N. L., Aiken, a C., Docherty, K. S., Ulbrich, I. M., Grieshop, a P., Robinson, a L., Duplissy, J.,  
509 Smith, J. D., Wilson, K. R., Lanz, V. a, Hueglin, C., Sun, Y. L., Tian, J., Laaksonen, a, Raatikainen, T., Rautiainen,  
510 J., Vaattovaara, P., Ehn, M., Kulmala, M., Tomlinson, J. M., Collins, D. R., Cubison, M. J., Dunlea, E. J., Huffman,  
511 J. a, Onasch, T. B., Alfarra, M. R., Williams, P. I., Bower, K., Kondo, Y., Schneider, J., Drewnick, F., Borrmann, S.,  
512 Weimer, S., Demerjian, K., Salcedo, D., Cottrell, L., Griffin, R., Takami, a, Miyoshi, T., Hatakeyama, S., Shimono,  
513 a, Sun, J. Y., Zhang, Y. M., Dzepina, K., Kimmel, J. R., Sueper, D., Jayne, J. T., Herndon, S. C., Trimborn, a M.,  
514 Williams, L. R., Wood, E. C., Middlebrook, a M., Kolb, C. E., Baltensperger, U. and Worsnop, D. R.: Evolution of  
515 organic aerosols in the atmosphere., *Science*, 326(5959), 1525–1529, doi:10.1126/science.1180353, 2009.

516 Kleinman, L. I.: Photochemical age determinations in the Phoenix metropolitan area, *J. Geophys. Res.*, 108(D3), 1–  
517 14, doi:10.1029/2002JD002621, 2003.

518 Kroll, J. H., Smith, J. D., Che, D. L., Kessler, S. H., Worsnop, D. R. and Wilson, K. R.: Measurement of  
519 fragmentation and functionalization pathways in the heterogeneous oxidation of oxidized organic aerosol., *Phys.*  
520 *Chem. Chem. Phys.*, 11(36), 8005–14, doi:10.1039/b905289e, 2009.

521 Kroll, J. H., Donahue, N. M., Jimenez, J. L., Kessler, S. H., Canagaratna, M. R., Wilson, K. R., Altieri, K. E.,  
522 Mazzoleni, L. R., Wozniak, A. S., Bluhm, H., Mysak, E. R., Smith, J. D., Kolb, C. E. and Worsnop, D. R.: Carbon  
523 oxidation state as a metric for describing the chemistry of atmospheric organic aerosol, *Nat. Chem.*, 3(2), 133–139,  
524 doi:10.1038/nchem.948, 2011.

525 Lambe, A. T., Onasch, T. B., Croasdale, D. R., Wright, J. P., Martin, A. T., Franklin, J. P., Massoli, P., Kroll, J. H.,  
526 Canagaratna, M. R., Brune, W. H., Worsnop, D. R. and Davidovits, P.: Transitions from Functionalization to  
527 Fragmentation Reactions of Laboratory Secondary Organic Aerosol (SOA) Generated from the OH Oxidation of  
528 Alkane Precursors, *Environ. Sci. Technol.*, 46(10), 5430–5437, doi:Doi 10.1021/Es300274t, 2012.

529 Lee, B. P., Li, Y. J., Yu, J. Z., Louie, P. K. K. and Chan, C. K.: Physical and chemical characterization of ambient  
530 aerosol by HR-ToF-AMS at a suburban site in Hong Kong during springtime 2011, *J. Geophys. Res. Atmos.*,  
531 118(15), 8625–8639, doi:10.1002/jgrd.50658, 2013a.

532 Lee, B. P., Li, Y. J., Flagan, R. C., Lo, C. and Chan, C. K.: Sizing Characterization of the Fast-Mobility Particle  
533 Sizer (FMPS) Against SMPS and HR-ToF-AMS, *Aerosol Sci. Technol.*, 47(9), 1030–1037,  
534 doi:10.1080/02786826.2013.810809, 2013b.

535 Li, Y., Pöschl, U. and Shiraiwa, M.: Molecular corridors and parameterizations of volatility in the chemical  
536 evolution of organic aerosols, *Atmos. Chem. Phys.*, 16(5), 3327–3344, doi:10.5194/acp-16-3327-2016, 2016.

537 Li, Y. J., Lee, B. Y. L., Yu, J. Z., Ng, N. L. and Chan, C. K.: Evaluating the degree of oxygenation of organic  
538 aerosol during foggy and hazy days in Hong Kong using high-resolution time-of-flight aerosol mass spectrometry  
539 (HR-ToF-AMS), *Atmos. Chem. Phys.*, 13(17), 8739–8753, doi:10.5194/acp-13-8739-2013, 2013.

540 Li, Y. J., Lee, B. P., Su, L., Fung, J. C. H. and Chan, C. K.: Seasonal characteristics of fine particulate matter (PM)  
541 based on high-resolution time-of-flight aerosol mass spectrometric (HR-ToF-AMS) measurements at the HKUST  
542 Supersite in Hong Kong, *Atmos. Chem. Phys.*, 15(1), 37–53, doi:10.5194/acp-15-37-2015, 2015.

543 LOUIE, P., WATSON, J., CHOW, J., CHEN, A., SIN, D. and LAU, A.: Seasonal characteristics and regional  
544 transport of PM in Hong Kong, *Atmos. Environ.*, 39(9), 1695–1710, doi:10.1016/j.atmosenv.2004.11.017, 2005.

545 Man, H., Zhu, Y., Ji, F., Yao, X., Lau, N. T., Li, Y., Lee, B. P. and Chan, C. K.: Comparison of daytime and  
546 nighttime new particle growth at the HKUST supersite in Hong Kong., *Environ. Sci. Technol.*, 49(12), 7170–8,  
547 doi:10.1021/acs.est.5b02143, 2015.

548 Mao, J., Ren, X., Brune, W. H., Olson, J. R., Crawford, J. H., Fried, A., Huey, L. G., Cohen, R. C., Heikes, B.,  
549 Singh, H. B., Blake, D. R., Sachse, G. W., Diskin, G. S., Hall, S. R. and Shetter, R. E.: Airborne measurement of  
550 OH reactivity during INTEX-B, *Atmos. Chem. Phys.*, 9(1), 163–173, doi:10.5194/acp-9-163-2009, 2009.

551 Mazzoleni, L. R., Ehrmann, B. M., Shen, X., Marshall, A. G. and Collett, J. L.: Water-Soluble Atmospheric Organic  
552 Matter in Fog: Exact Masses and Chemical Formula Identification by Ultrahigh-Resolution Fourier Transform Ion  
553 Cyclotron Resonance Mass Spectrometry, *Environ. Sci. Technol.*, 44(10), 3690–3697, doi:10.1021/es903409k, 2010.

554 Meng, J. W., Yeung, M. C., Li, Y. J., Lee, B. Y. L. and Chan, C. K.: Size-resolved cloud condensation nuclei (CCN)  
555 activity and closure analysis at the HKUST Supersite in Hong Kong, *Atmos. Chem. Phys.*, 14(18), 10267–10282,  
556 doi:10.5194/acp-14-10267-2014, 2014.

557 Mohr, C., DeCarlo, P. F., Heringa, M. F., Chirico, R., Slowik, J. G., Richter, R., Reche, C., Alastuey, A., Querol, X.,  
558 Seco, R., Peñuelas, J., Jimenez, J. L., Crippa, M., Zimmermann, R., Baltensperger, U., Prevôt, A. S. H.,  
559 Peñuelas, J., Jiménez, J. L., Crippa, M., Zimmermann, R., Baltensperger, U. and Prevôt, A. S. H.: Identification and  
560 quantification of organic aerosol from cooking and other sources in Barcelona using aerosol mass spectrometer data,  
561 *Atmos. Chem. Phys.*, 12(4), 1649–1665, doi:10.5194/acp-12-1649-2012, 2012.

562 Ng, N. L., Canagaratna, M. R., Jimenez, J. L., Chhabra, P. S., Seinfeld, J. H. and Worsnop, D. R.: Changes in  
563 organic aerosol composition with aging inferred from aerosol mass spectra, *Atmos. Chem. Phys.*, 11(13), 6465–  
564 6474, doi:10.5194/acp-11-6465-2011, 2011.

565 Petäjä, T., Järvi, L., Kerminen, V.-M., Ding, A. J., Sun, J. N., Nie, W., Kujansuu, J., Virkkula, A., Yang, X., Fu, C.  
566 B., Zilitinkevich, S. and Kulmala, M.: Enhanced air pollution via aerosol-boundary layer feedback in China., *Sci.*  
567 *Rep.*, 6, 18998, doi:10.1038/srep18998, 2016.

568 Seinfeld, J. H. and Pandis, S. N.: *ATMOSPHERIC From Air Pollution to Climate Change SECOND EDITION.*,  
569 2006.

570 Shiraiwa, M., Yee, L. D., Schilling, K. a, Loza, C. L., Craven, J. S., Zuend, A., Ziemann, P. J. and Seinfeld, J. H.:  
571 Size distribution dynamics reveal particle-phase chemistry in organic aerosol formation., *Proc. Natl. Acad. Sci. U. S.*  
572 *A.*, 110(29), 11746–50, doi:10.1073/pnas.1307501110, 2013.

573 Squizzato, S., Masiol, M., Brunelli, a., Pistollato, S., Tarabotti, E., Rampazzo, G. and Pavoni, B.: Factors  
574 determining the formation of secondary inorganic aerosol: A case study in the Po Valley (Italy), *Atmos. Chem.*  
575 *Phys.*, 13(4), 1927–1939, doi:10.5194/acp-13-1927-2013, 2013.

576 Su, L., Yuan, Z., Fung, J. C. H. and Lau, A. K. H.: A comparison of HYSPLIT backward trajectories generated from  
577 two GDAS datasets, *Sci. Total Environ.*, 506–507, 527–537, doi:10.1016/j.scitotenv.2014.11.072, 2015.

578 Takegawa, N., Miyakawa, T., Kondo, Y., Blake, D. R., Kanaya, Y., Koike, M., Fukuda, M., Komazaki, Y.,  
579 Miyazaki, Y., Shimono, a. and Takeuchi, T.: Evolution of submicron organic aerosol in polluted air exported from  
580 Tokyo, *Geophys. Res. Lett.*, 33(15), 3–7, doi:10.1029/2006GL025815, 2006.

581 Volkamer, R., Jimenez, J. L., San Martini, F., Dzepina, K., Zhang, Q., Salcedo, D., Molina, L. T., Worsnop, D. R.  
582 and Molina, M. J.: Secondary organic aerosol formation from anthropogenic air pollution: Rapid and higher than  
583 expected, *Geophys. Res. Lett.*, 33(17), L17811, doi:10.1029/2006GL026899, 2006.

584 Wang, Y., Zhuang, G., Tang, A., Yuan, H., Sun, Y., Chen, S. and Zheng, A.: The ion chemistry and the source of  
585 PM<sub>2.5</sub> aerosol in Beijing, *Atmos. Environ.*, 39(21), 3771–3784, doi:10.1016/j.atmosenv.2005.03.013, 2005.

586 Yeung, M. C., Lee, B. P., Li, Y. J. and Chan, C. K.: Simultaneous HTDMA and HR-ToF-AMS measurements at the  
587 HKUST Supersite in Hong Kong in 2011, *J. Geophys. Res. Atmos.*, 119(16), 9864–9883,  
588 doi:10.1002/2013JD021146, 2014.

589 Zhang, Q., Jimenez, J. L., Canagaratna, M. R., Ulbrich, I. M., Ng, N. L., Worsnop, D. R. and Sun, Y.:  
590 Understanding atmospheric organic aerosols via factor analysis of aerosol mass spectrometry: A review, *Anal.*  
591 *Bioanal. Chem.*, 401(10), 3045–3067, doi:10.1007/s00216-011-5355-y, 2011.

592 Zhang, R., Wang, G., Guo, S., Zamora, M. L., Ying, Q., Lin, Y., Wang, W., Hu, M. and Wang, Y.: Formation of  
593 Urban Fine Particulate Matter, *Chem. Rev.*, 115(10), 3803–3855, doi:10.1021/acs.chemrev.5b00067, 2015a.

594 Zhang, Y. W., Zhang, X. Y., Zhang, Y. M., Shen, X. J., Sun, J. Y., Ma, Q. L., Yu, X. M., Zhu, J. L., Zhang, L. and  
595 Che, H. C.: Significant concentration changes of chemical components of PM1 in the Yangtze River Delta area of  
596 China and the implications for the formation mechanism of heavy haze-fog pollution., *Sci. Total Environ.*, 538, 7–  
597 15, doi:10.1016/j.scitotenv.2015.06.104, 2015b.

598 Zhao, Y., Hallar, A. G. and Mazzoleni, L. R.: Atmospheric organic matter in clouds: exact masses and molecular  
599 formula identification using ultrahigh-resolution FT-ICR mass spectrometry, *Atmos. Chem. Phys.*, 13(24), 12343–  
600 12362, doi:10.5194/acp-13-12343-2013, 2013.

601 Zhong, L., Louie, P. K. K., Zheng, J., Yuan, Z., Yue, D., Ho, J. W. K. and Lau, A. K. H.: Science–policy interplay:  
602 Air quality management in the Pearl River Delta region and Hong Kong, *Atmos. Environ.*, 76, 3–10,  
603 doi:10.1016/j.atmosenv.2013.03.012, 2013.

604 Zhou, S., Wang, T., Wang, Z., Li, W., Xu, Z., Wang, X., Yuan, C., Poon, C. N., Louie, P. K. K., Luk, C. W. Y. and  
605 Wang, W.: Photochemical evolution of organic aerosols observed in urban plumes from Hong Kong and the Pearl  
606 River Delta of China, *Atmos. Environ.*, 88, 219–229, doi:10.1016/j.atmosenv.2014.01.032, 2014.

607

**Tables:**

*Table 1 Synopsis of meteorological conditions of high PM episodes*

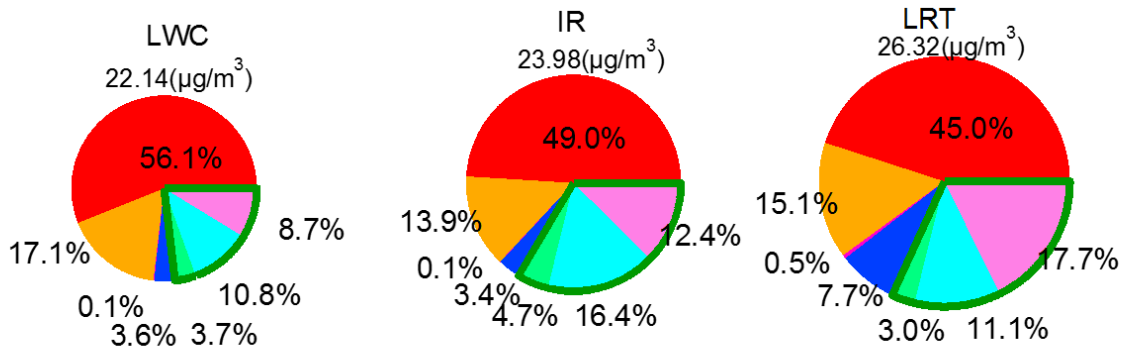
Episode	Season	Date	Air mass origin	Wind speed (m s <sup>-1</sup> )	Solar Irradiance (w m <sup>-2</sup> )	Liquid water content (µg m <sup>-3</sup> )	PM <sub>1</sub> (µg m <sup>-3</sup> )	PM <sub>1</sub> Max (µg m <sup>-3</sup> )	Type
E1	Spring	28-30 Apr	M-R <sup>a</sup> /NE <sup>b</sup>	0.7±0.4	41±67	47.1±15.9	25.5±3.1	33.1	LWC
E2	Spring	14-16 May	M-R/NE <sup>b</sup>	1.1±0.8	27±61	38.6±14.5	18.8±6.4	32.4	LWC
E3	Spring	27-29 May	M-R <sup>a</sup> /NE <sup>b</sup>	0.9±0.8	184±263	19.3±9.2	28.4±12.6	64.1	IR
E4	Summer	2 Sep	M-R <sup>a</sup> /NW <sup>b</sup>	0.5±0.4	111±163	20.0±3.1	22.5±6.1	33.7	IR
E5	Summer	20-24 Sep	M-R <sup>a</sup> /NE <sup>b</sup>	2.2±0.5	143±234	14.9±4.6	23.8±4.8	35.9	IR
E6	Autumn	3 Nov	M-R <sup>a</sup> /NE <sup>b</sup>	1.3±0.5	174±271	12.8±5.9	15.6±6.2	30.0	IR
E7	Autumn	13-15 Nov	M-R <sup>a</sup> /NE <sup>b</sup>	1.2±0.5	150±221	19.4±7.0	23.4±7.0	45.2	IR
E8	Winter	24-25 Nov	L-R <sup>a</sup> /NE <sup>b</sup>	1.6±0.5	112±174	14.1±6.6	25.9±6.2	38.6	LRT
E9	Winter	8 Feb	L-R <sup>a</sup> /N <sup>b</sup>	2.2±0.6	49±74	27.8±2.8	29.7±8.1	41.6	LRT
E10	Winter	18-19 Feb	L-R <sup>a</sup> /NE <sup>b</sup>	1.5±0.6	104±170	16.0±5.3	25.5±9.4	64.9	LRT

**a: Range of air mass origin: Medium range (M-R); Long range (L-R).**  
**b: Direction of air mass origin: Northeast (NE); Northwest(NW); North (N).**



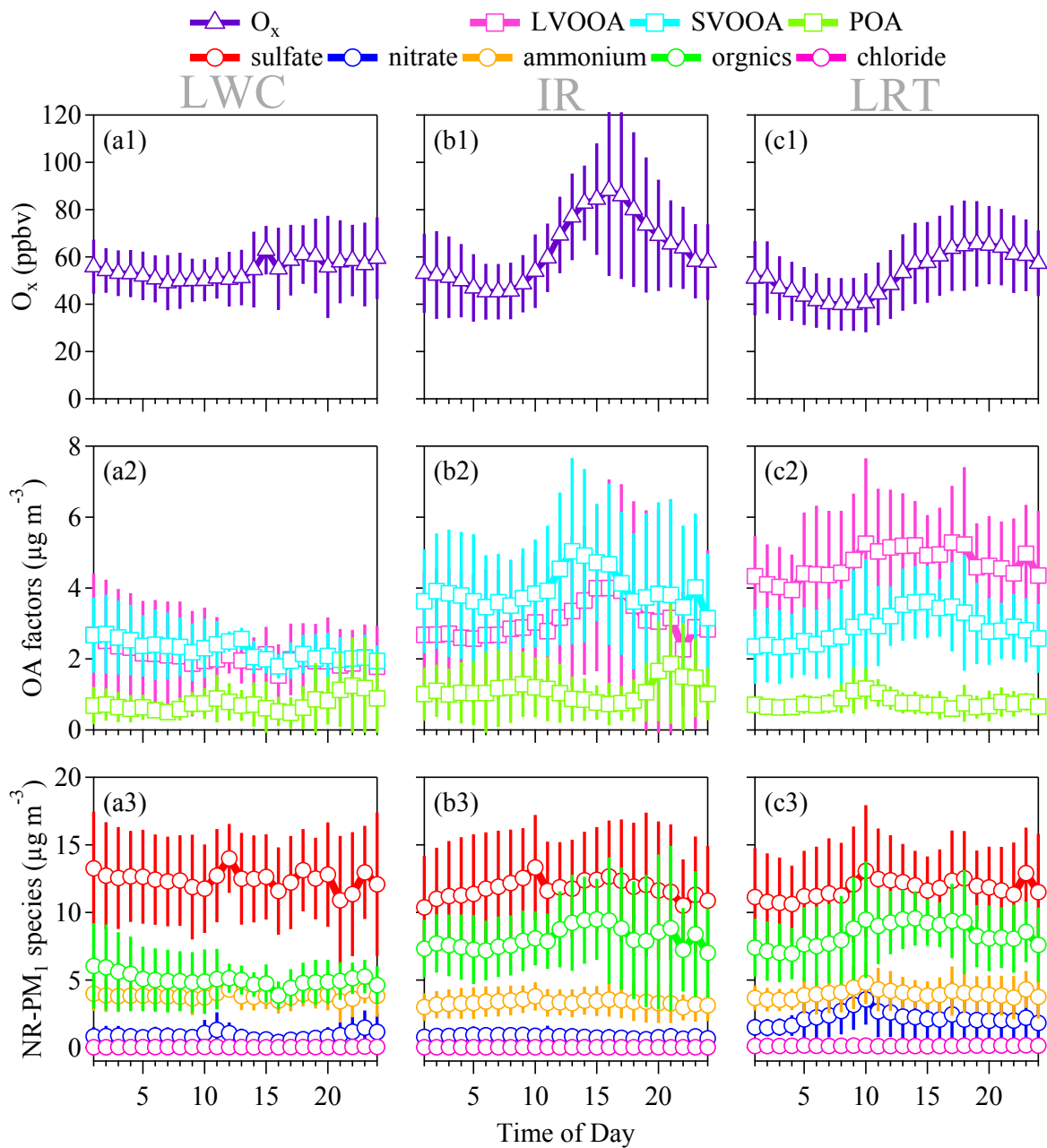
1 **Figures:**

Sulfate Nitrate Ammonium Chloride Organic (POA, SVOOA, LVOOA)



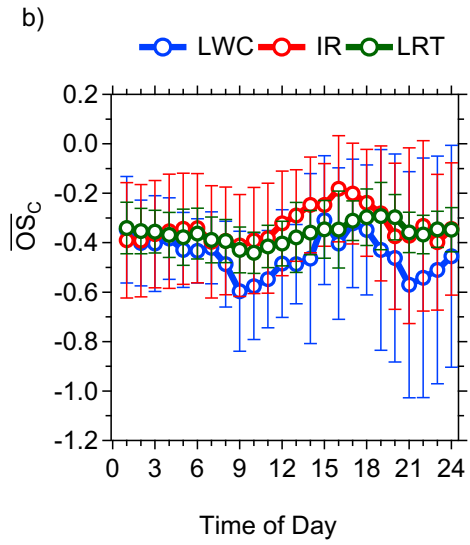
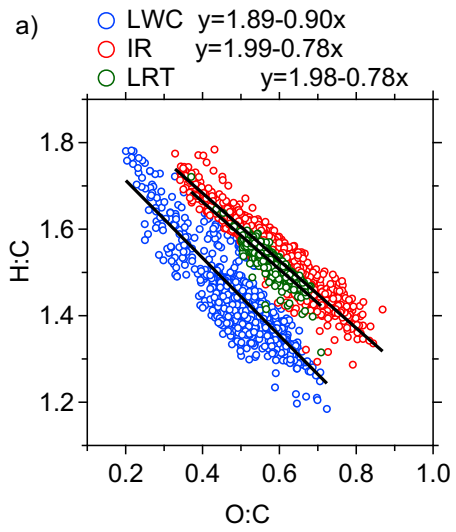
2

3 *Figure 1 Chemical constituents NR-PM<sub>1</sub> in LWC, IR and LRT episodes. (LWC: medium-range transport with high*  
4 *LWC and low IR; IR: medium-range transport with high IR and low LWC; LRT: long-range transport)*



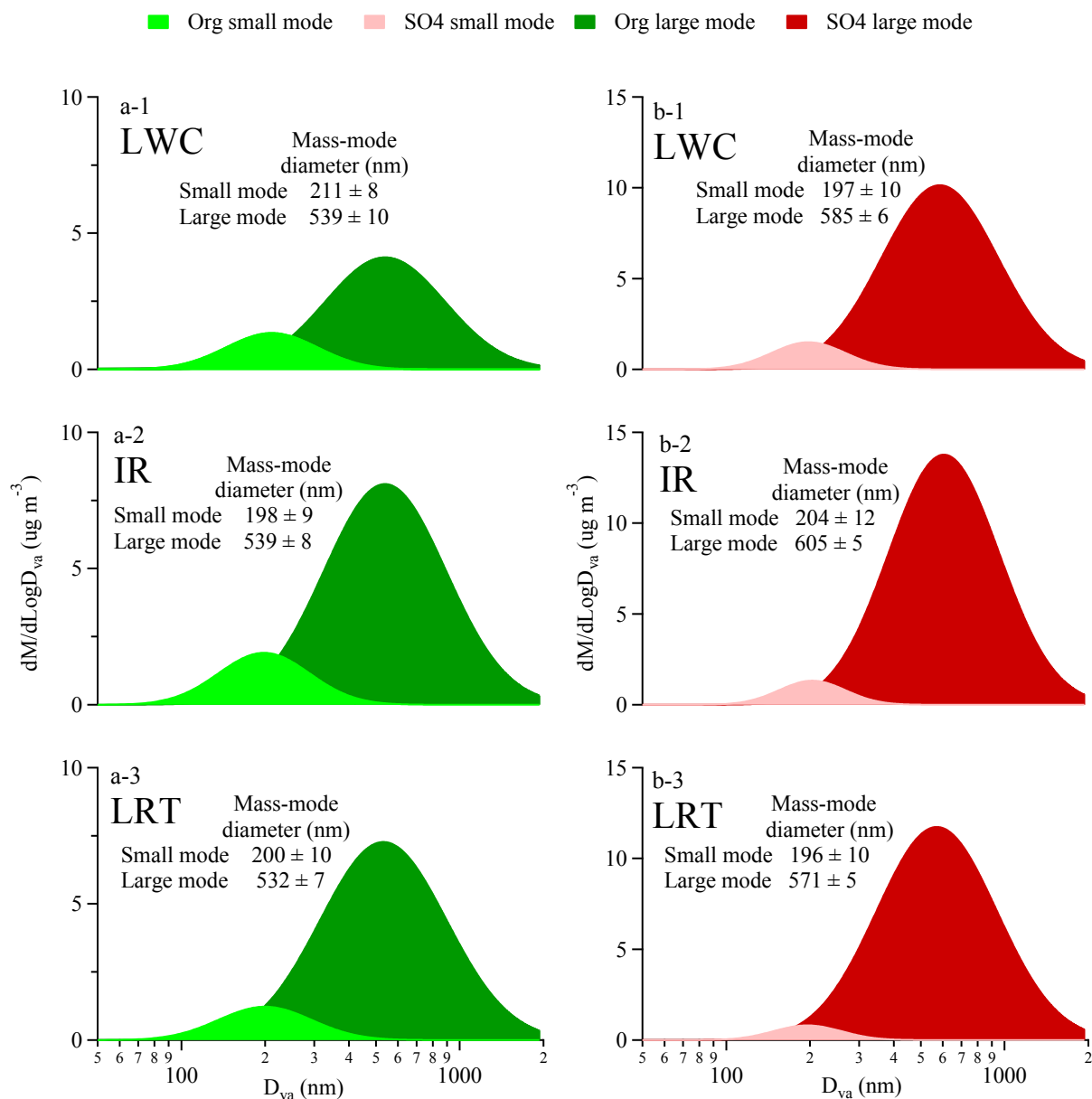
5

6 Figure 2 Summary of diurnal variations of the  $PM_1$  species, PMF-resolved organics as well as  $O_x$  in the three types  
 7 of episodes. Means are shown as points and standard deviations are as error bars.



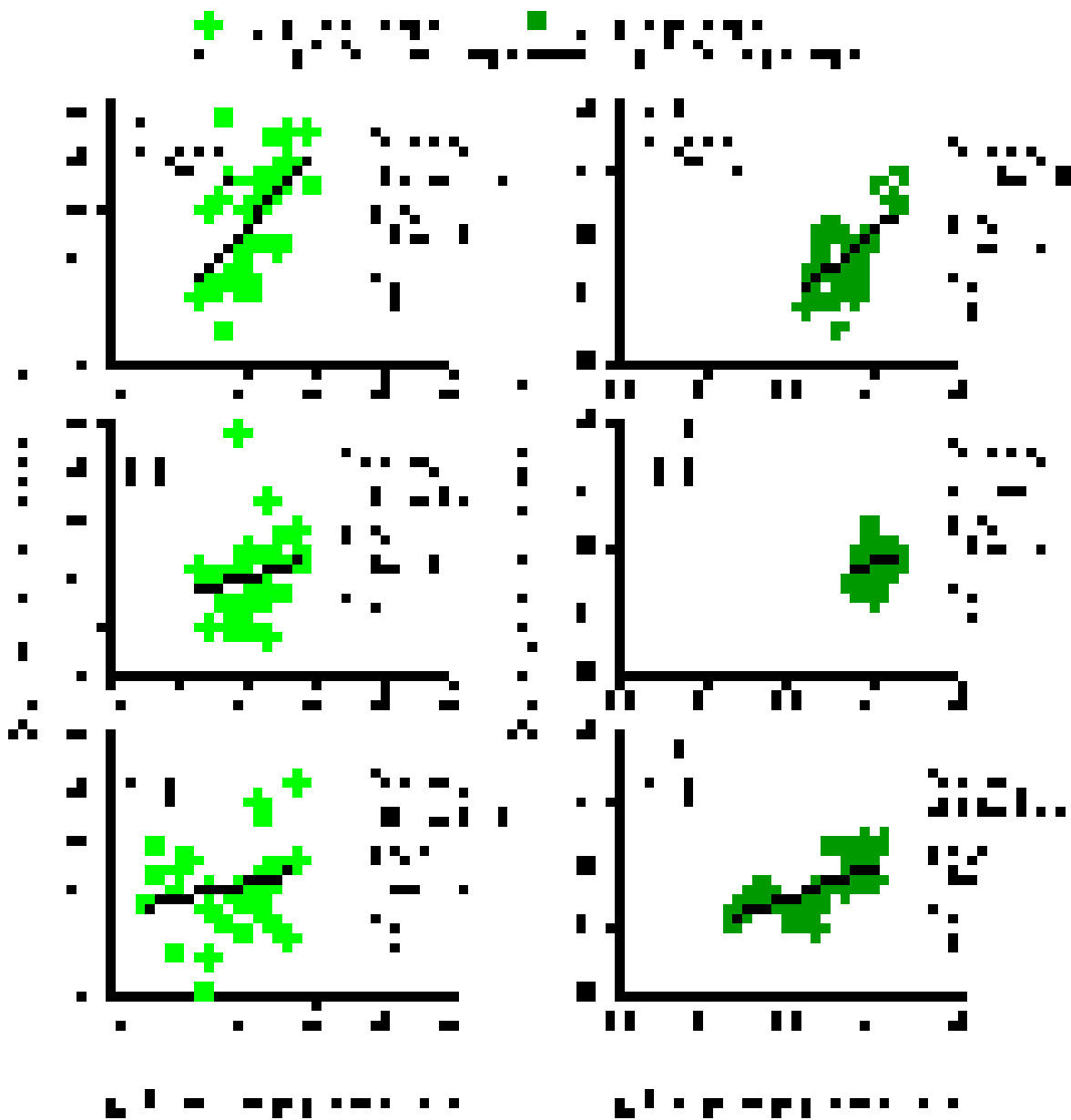
8

9 *Figure 3 a) Van Krevelen diagram for the three types of episodes; b) diurnal variation of carbon oxidation state*  
 10 *( $\overline{OS}_c$ ). Means appear as circles with superimposed standard deviations.*



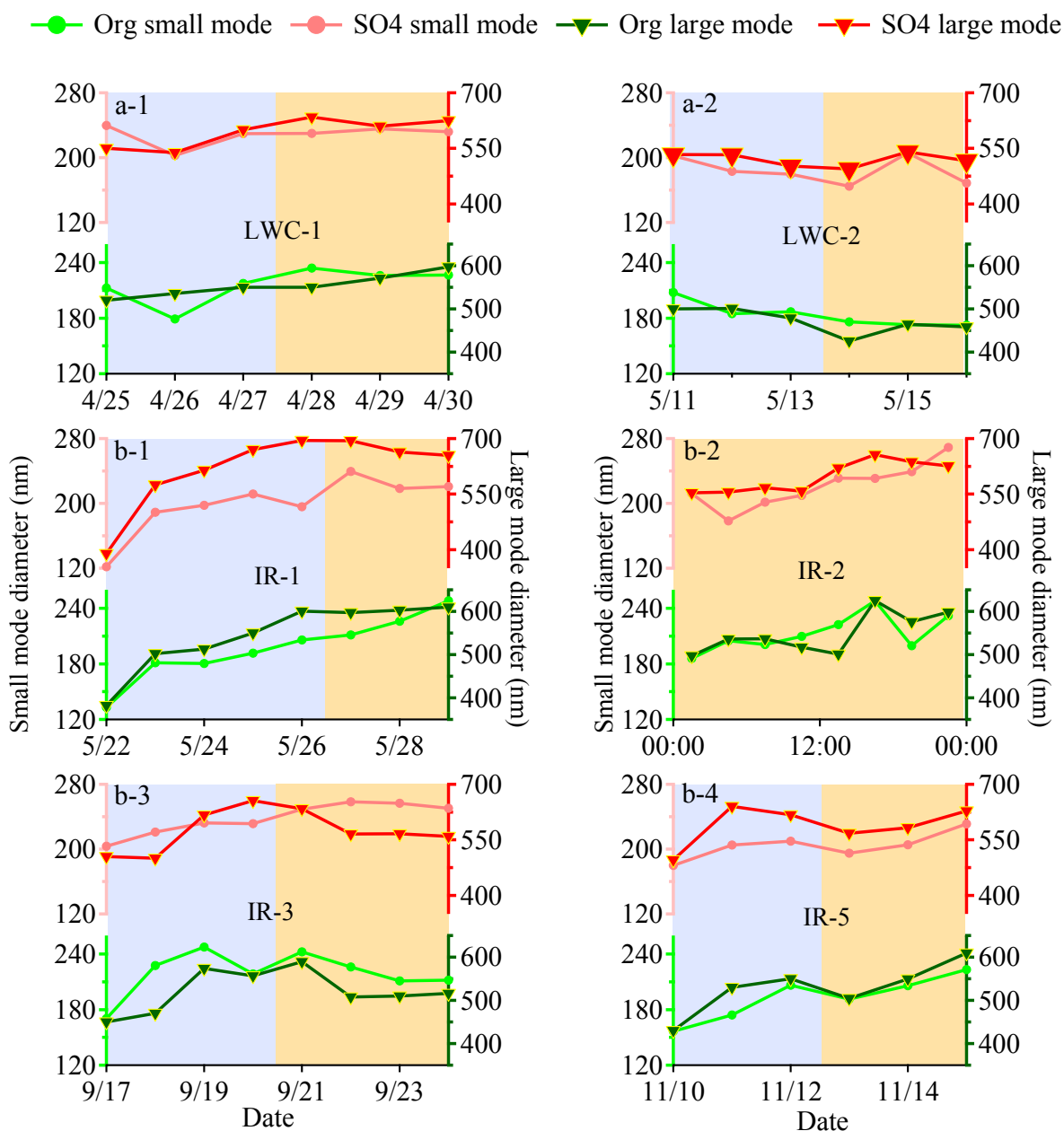
11

12 *Figure 4 Bimodal log-normal fitting results of the size distributions of organics and sulfate during the three types of*  
 13 *episodes. a) Fitted small particle size mode and large particle size mode of organics during LWC, IR and LRT*  
 14 *episodes; b) fitted small particle size mode and large particle size mode of sulfate during LWC, IR and LRT episodes.*



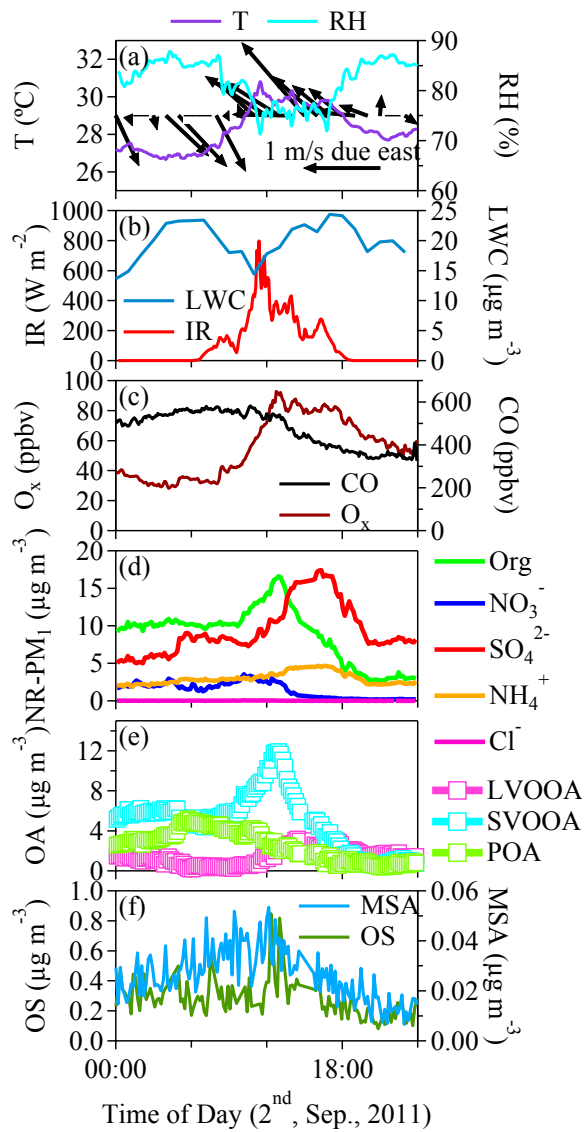
15

16 *Figure 5 Scatter plots and linear least square fits of mass-mode diameters of organics and sulfate during the three*  
 17 *different types of episodes. a1-a2) small and large mass-mode diameter of organics against sulfate during LWC*  
 18 *episodes; b1-b2) small and large mass-mode diameter of organics against sulfate during IR episodes; c1-c2) small*  
 19 *and large mass-mode diameter of organics against sulfate during LRT episodes.*



20

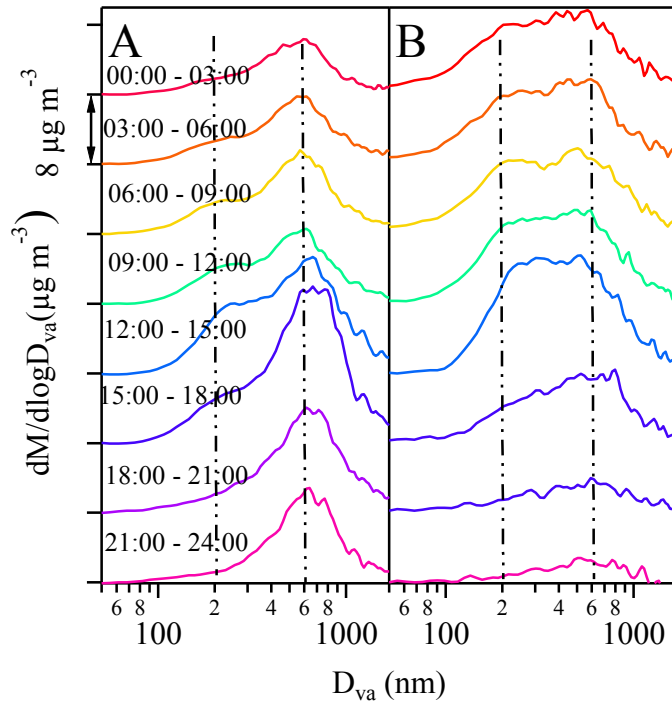
21 *Figure 6 Variations of 24-hour averaged size distributions of fitted mass-mode diameters of organics and sulfates*  
 22 *during LWC episodes and IR episodes (shaded in orange) and several days before each episode (shaded in blue).*  
 23 *For the episode that lasted only for a day (E4), 3-hour averaged size distributions of fitted mass-mode diameters are*  
 24 *shown instead. a) LWC episodes; b) IR episodes.*



25

26 *Figure 7 Time series of meteorological parameters, gaseous species, NR-PMI species and PMF-resolved organic*  
 27 *factors in E4.*

# Sulfate Organics

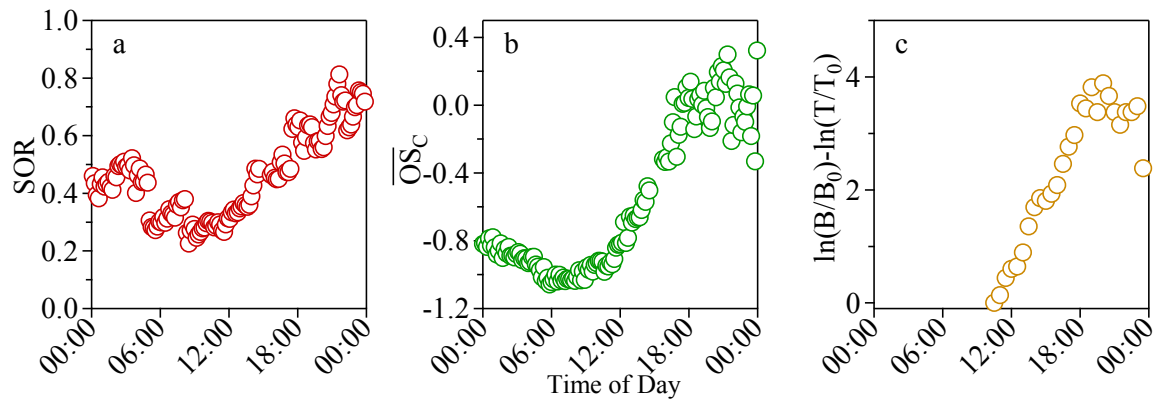


28

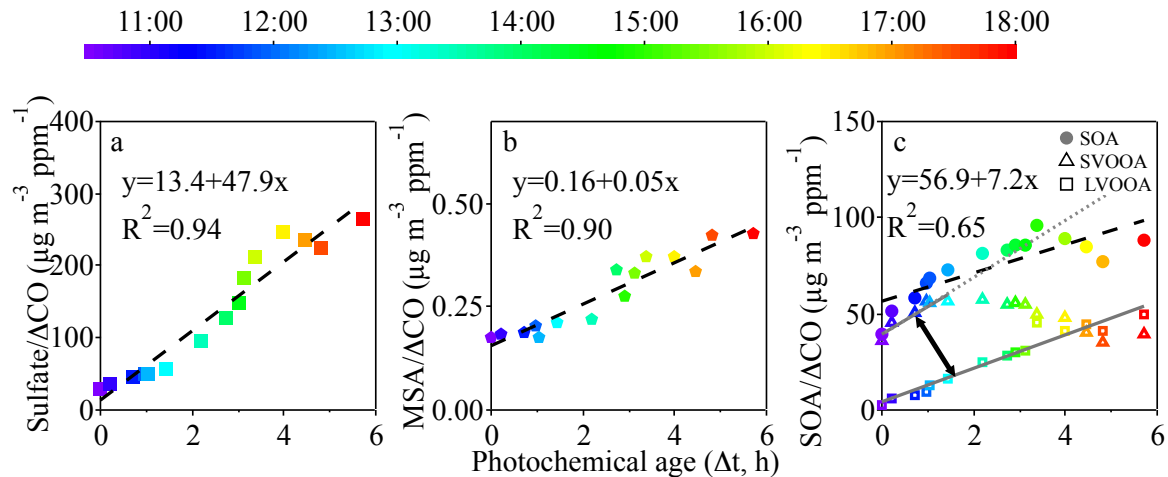
29 *Figure 8 Size distributions of sulfate (A) and organics (B) in different time intervals during E4.*



30

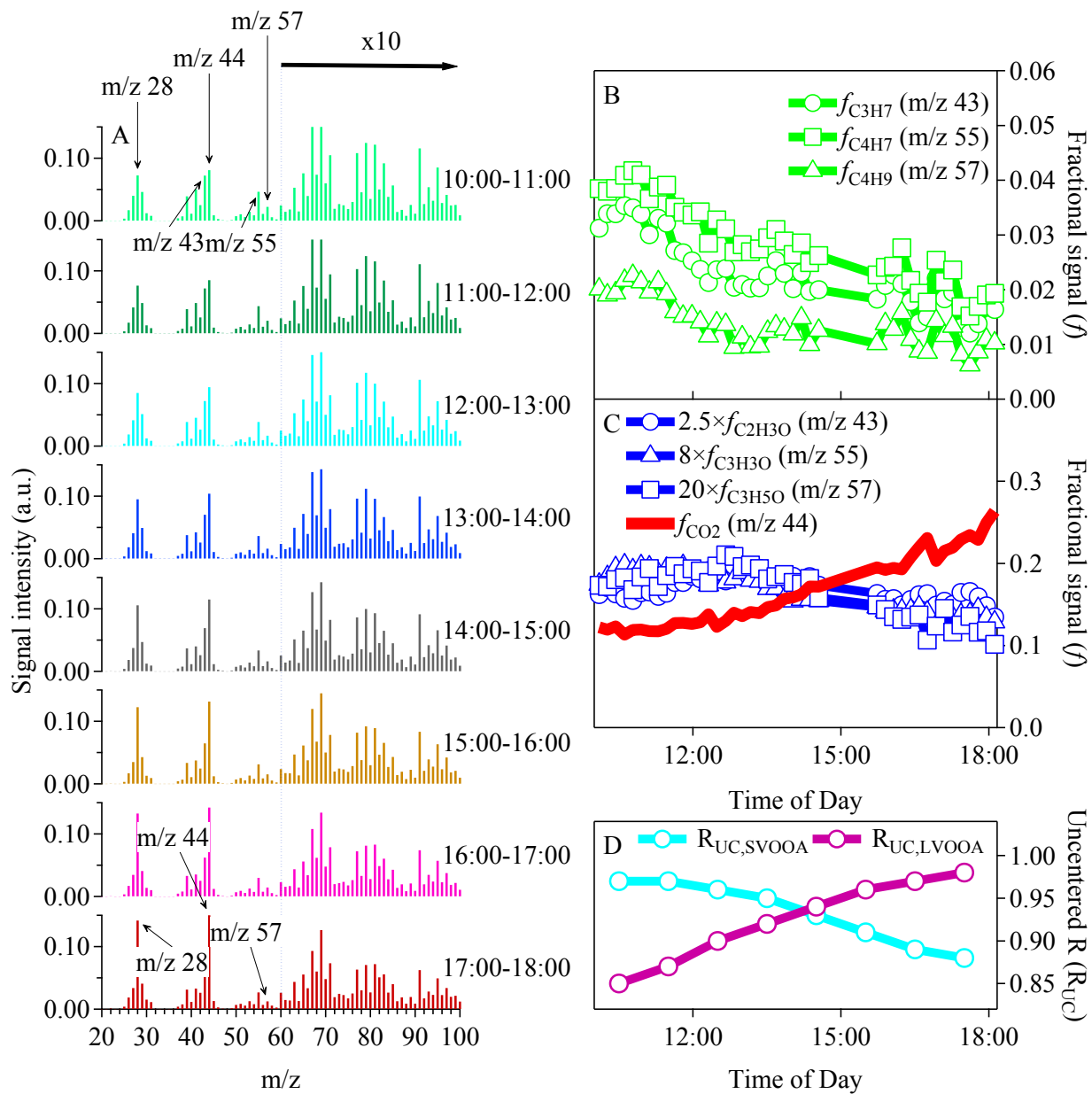


31 *Figure 9 Oxidative evolution of aerosol components. a) Sulfur oxidation ratio (SOR); b) average carbon oxidation*  
32 *state  $\overline{OS}_c$ ; c) benzene to toluene ratio (B: benzene concentration at time t; B0: benzene concentration at time 0; T:*  
33 *toluene concentration at time t; T0: toluene concentration at time 0).*



34

35 *Figure 10 Photochemical production of secondary species. a)  $\Delta\text{CO}$ -normalized sulfate concentration ( $\text{SO}_4/\Delta\text{CO}$ )*  
 36 *as a function of photochemical age; b)  $\Delta\text{CO}$ -normalized MSA concentration ( $\text{MSA}/\Delta\text{CO}$ ) as a function of*  
 37 *photochemical age; and c)  $\Delta\text{CO}$ -normalized secondary organic aerosol concentration ( $\text{SOA}/\Delta\text{CO}$ ,*  
 38  *$\text{SOA}(\text{SVOOA}+\text{LVOOA})$ ) as a function of photochemical age. Data points are colored by time of day. Data points*  
 39 *represent half-hour averages.*



40

41 *Figure 11 Evolution of high-resolution organic mass spectra from 10:00 to 18:00 during the photochemical aging*  
 42 *process in E4: a) mass spectral evolution; b) changes in relative intensities of hydrocarbon-like ions  $C_3H_7^+$  ( $m/z$  43),*  
 43  *$C_4H_7^+$  ( $m/z$  55) and  $C_4H_9^+$  ( $m/z$  57); c) changes in relative intensities of oxygen-containing ions:  $C_2H_3O^+$  ( $m/z$  43),*  
 44  *$C_3H_3O^+$  ( $m/z$  55),  $C_3H_5O^+$  ( $m/z$  57) and  $CO_2^+$  ( $m/z$  44); and d) correlation of OA mass spectra with reference (Mohr et*  
 45 *al., 2012) SVOOA and LVOOA mass spectra.*